JOURNAL OF GEOPHYSICAL RESEARCH, VOL. 106, NO. C10, PAGES 22,475–22,502, OCTOBER 15, 2001

Estimates of M_2 tidal energy dissipation from TOPEX/Poseidon altimeter data

Gary D. Egbert

College of Oceanic and Atmospheric Sciences, Oregon State University, Corvallis, Oregon, USA

Richard D. Ray

NASA Goddard Space Flight Center, Greenbelt, Maryland, USA

Abstract. Most of the tidal energy dissipation in the ocean occurs in shallow seas, as has long been recognized. However, recent work has suggested that a significant fraction of the dissipation, perhaps 1 TW or more, occurs in the deep ocean. This paper builds further evidence for that conclusion. More than 6 years of data from the TOPEX/Poseidon satellite altimeter are used to map the tidal dissipation rate throughout the world ocean. The dissipation rate is estimated as a balance between the rate of working by tidal forces and the energy flux divergence, computed using currents derived by least squares fitting of the altimeter data and the shallow water equations. Such calculations require dynamical assumptions, in particular about the nature of dissipation. To assess sensitivity of dissipation estimates to input assumptions, a large suite of tidal inversions based on a wide range of drag parameterizations and employing both real and synthetic altimeter data are compared. These experiments and Monte Carlo error fields from a generalized inverse model are used to establish error uncertainties for the dissipation estimates. Owing to the tight constraints on tidal elevation fields provided by the altimeter, area integrals of the energy balance are remarkably insensitive to required dynamical assumptions. Tidal energy dissipation is estimated for all major shallow seas (excluding individual polar seas) and compared with previous model and data-based estimates. Dissipation in the open ocean is significantly enhanced around major bathymetric features, in a manner consistent with simple theories for the generation of baroclinic tides.

1. Introduction

The problem of how and where the tides dissipate their energy was listed by *Wunsch* [1990, p. 69] as one of four "significant hard problems [in physical oceanography] to be solved in the next century." The problem certainly has a long and frustrating history. That it continues to attract attention is a reflection of both its intrinsic fascination and its importance. The geophysical implications are far-reaching, ranging from the history of the Moon [*Hansen*, 1982] to the mixing of the oceans [*Munk*, 1997].

In a recent short paper [*Egbert and Ray*, 2000] (hereinafter referred to as E-R] we addressed the problem in light of accurate global estimates of tidal elevations made available by the TOPEX/Poseidon (T/P) satellite altimeter. That paper concludes that approximately 1 terawatt (TW), or 25–30% of the global total, is dissipated in the deep oceans. The present paper reexamines the subject with considerably more thorough analysis of both data and methods, and it builds further evidence for the basic conclusions in E-R. Like our earlier work the present paper addresses the questions of "how much" and "where" tidal energy is dissipated, but not "how." Yet the answer to "where" holds some obvious suggestions as to "how."

The total amount of tidal energy being dissipated in the Earth-Moon-Sun system is now well determined. The methods of space geodesy—altimetry, satellite laser ranging, lunar laser ranging—have converged to 3.7 TW, with 2.5 TW (for more precision and error bars, see below) for the principal lunar tide M_2 [*Cartwright*, 1993; *Ray*, 1994; *Kagan and Sündermann*, 1996]. Certainly, the bulk of this energy dissipation occurs in the oceans. And within the oceans the principal sink is most likely bottom boundary layer dissipation in shallow seas, the traditional explanation since the work of *Jeffreys* [1920]. There is much evidence to support this view [*Munk*, 1997], including long experience with hydrodynamic models [*Le Provost and Lyard*, 1997] and our own recent estimates from satellite altimetry (E-R). Another possible energy sink, conversion of energy into internal tides and other baroclinic waves, has long attracted attention but has proven extremely difficult to quantify [*Wunsch*, 1975]. *Baines* [1982; see also *Huthnance*, 1989] concluded that generation of internal tides at the continental slopes is an insignificant sink (approximately 12 GW for M_2 over the en-

Paper number 2000JC000699.
0148-0227/2000JC000699$09.00

tire globe). But scattering by deep-ocean bottom topography may be more important than generation at continental slopes [*Sjöberg and Stigebrandt*, 1992; *Morozov*, 1995]. The possible importance of this mechanism to deep-ocean mixing has recently been discussed by *Munk and Wunsch* [1998].

As is well known [e.g., *Lambeck*, 1977; *Platzman*, 1984], global charts of tidal elevations suffice to determine the global rate of working of tidal forces on the ocean (see also section 2). To deduce localized estimates of energy fluxes and energy dissipation requires corresponding charts of tidal current velocities. Direct measurements of currents are, of course, inadequate to the task; they are too sparse, generally too noisy, and often contaminated by baroclinic effects. To make progress, one must invoke dynamics to infer currents from elevations, and this unfortunately means making assumptions about dissipation. The problem appears inherently circular.

Assessing the degree to which dissipation estimates can be made insensitive to dynamical assumptions is the heart of the problem. It should be clear that simply fitting a numerical tide model to satellite measurements and evaluating the model's dissipative terms is too simplistic an approach. The resulting dissipation would be overly sensitive to model assumptions and parameterizations. For example, using the typical bottom drag dissipation (parameterized as quadratic in velocity) would force all dissipation into shallow seas for any plausible specification of friction coefficients.

The basic approach taken in E-R and here is to estimate currents by fitting the dynamical equations and the T/P elevations using weighted least squares, calculate energy fluxes, and then form a balance between the rate of working of tidal forces and the flux divergence. In general, the results of this calculation will not equal the dissipation in the assumed dynamical model, because the tidal elevations are tightly constrained to satisfy the satellite observations and therefore cannot, in general, also exactly satisfy the model equations. The implied "dynamical residuals" are in some sense an additional forcing term whose working corrects the assumed dissipation to be consistent with the altimetrically constrained elevations (see below) [*Zahel*, 1995; *Egbert*, 1997]. We show here that with sufficiently tight elevation constraints and rational weighting of the momentum and mass conservation equations, dissipation maps computed with this approach are robust to a wide range of dynamical assumptions. The near-global tidal observations by T/P thus provide a powerful framework for addressing the dissipation problem.

These ideas are discussed at length in section 5, where the main results are given. Sections 2–4 establish necessary preliminaries. Section 2 reviews the data and theories that constrain the total energy dissipation rate in the ocean; any localized dissipation estimates must integrate to these well-determined global totals. Section 3, following primarily *Hendershott* [1972], forms energy balance equations used for localized dissipation estimates, and it reviews how various terms simplify when inserted into surface integrals. Because of the wide variety of energy balance equations that have been used in the past, we find it useful to reexamine some work and flux terms from first principles. Section 4 provides a brief overview of the methods used for estimating tidal currents from the T/P elevations. In section 5 we provide estimates of energy fluxes, work terms, and dissipation derived from a number of T/P tidal solutions, including a complete tabulation of estimates of energy fluxes into all shallow seas, and dissipation in selected deep-ocean areas. In this section we also consider in detail the sensitivity of our results to the prior assumptions about dissipation and bathymetry required to estimate currents. Section 6 compares our estimates of shallow-sea dissipation to empirical and model estimates from a number of previous authors. The geophysical implications of our results are briefly explored in section 7.

As in E-R, discussion is limited to the principal lunar constituent M_2. The principal solar constituent S_2 is confounded by insolation and atmospheric effects that considerably complicate the main issue, while the major diurnal tides are less well determined. As noted above, M_2 accounts for approximately two thirds of the total tidal dissipation.

2. Global Dissipation Rate for Earth and Oceans

The primary purpose of this paper is to determine empirically the distribution of tidal energy dissipation in the world ocean. The present section is a prologue, acting to establish the total dissipation rate within the entire planet and the partition of this total among the solid Earth, oceans, and atmosphere. We review what kinds of measurements or theories constrain the partition and what the current uncertainties are. The partitioning is not as accurately known as the planetary total.

2.1. Planetary Dissipation Rate

The theory of the planetary tidal dissipation was laid out in comprehensive and elegant form by *Platzman* [1984]. We take it as axiomatic that the mean planetary dissipation rate equals the mean rate of working by tidal forces throughout the planet. Platzman showed that this rate of working can be expressed as a simple surface integral involving the primary astronomical potential Φ and the secondary (induced) potential Φ', the latter resulting from tidal displacements within the solid and fluid components of the Earth. For any semidiurnal tide like M_2 the integral takes the following form:

$$D_{\text{total}} = W_{\text{total}} = (5/4\pi GR) \int_S \langle \Phi \, \partial\Phi'/\partial t \rangle \, dS, \qquad (1)$$

where G is the gravitational constant and R is the mean radius of the Earth which forms the surface S. The angle brackets denote averaging in time over a tidal cycle. As Platzman points out, the simplicity of (1) is somewhat deceptive, because disentangling and understanding the components of Φ' requires a mixture of theory and accurate global measurements which, although much improved since Platzman's work in 1984, are still in some measure inadequate to the task.

We suppose that both potentials Φ and Φ' refer to M_2 only. Then Φ is a degree 2, order 2 spherical harmonic [*Cartwright and Tayler*, 1971]

$$\Phi(\theta, \varphi, t) = g\tilde{H}\sqrt{(5/96\pi)}\, P_2^2(\cos\theta)\, \cos(\omega t + 2\varphi),$$

where (θ, φ) are spherical polar coordinates, g is the acceleration of gravity, P_2^2 is an associated Legendre function, ω is the M_2 frequency (1.405×10^{-4} s^{-1}), and $\tilde{H}$ is the M_2 potential amplitude in length units (63.194 cm). Because Φ takes this form, time averaging in (1) and the orthogonality of spherical harmonics imply that evaluation of D_{total} requires only the degree 2, order 2 component of Φ' that is in quadrature to Φ [cf. *Hendershott*, 1972; *Lambeck*, 1977; *Platzman*, 1984].

The most direct route to determining Φ' is by analyzing the orbital perturbations of artificial satellites, which result from forcing by the entire planetary potential. The order 2 terms of Φ', which include the one of interest here, are especially well determined for semidiurnal tides, because they induce long-period perturbations that are easily observable with present tracking systems [*Lambeck*, 1977].

Although Φ' is a combined (solid + ocean + air) effect, nearly all published orbit analyses parameterize Φ' as if it arises from a strictly elastic body tide and a small residual ocean tide [e.g., *Christodoulidis et al.*, 1988]. This parameterization, although formally incorrect, does reflect the dominant tidal forces on a satellite, and it provides a fully satisfactory estimate of Φ' needed for evaluating (1) numerically. The potential due to the ocean tide is usefully expressed in terms of a series of waves, each a spherical harmonic component of some unique degree and order. As noted above, we require here only one of these waves: the degree 2, order 2 prograde ("prograde" meaning moving in the direction of the Moon). Then for our purposes Φ' reduces to

$$\Phi' = k_2\Phi + (4\pi/5)GR\rho(1 + k_2') \times P_2^2(\cos\theta)\, D_{22}^+ \cos(\omega t + 2\varphi - \psi_{22}^+). \quad (2)$$

The first term on the right is the potential induced by deformations of the body tide, the second by deformations of the ocean tide and its load. Here k_2 is the body tide Love number, k_2' is the degree 2 loading number, and ρ is the density of seawater. Nominal, real values for k_2, k_2' are assumed in most orbit analyses, with the effect of anelasticity of the solid Earth (as well as all atmospheric tides) absorbed into the ocean tide amplitude D_{22}^+ and phase lag ψ_{22}^+ through fitting to the tracking data. Inserting (2) with real k_2, k_2' into (1) and setting $gR^2 = GM$ where M is the mass of the Earth yields

$$D_{\text{total}} = \rho(1 + k_2')\omega GM\tilde{H}(24\pi/5)^{1/2} D_{22}^+ \sin\psi_{22}^+, \quad (3)$$

an expression allowing evaluation of the planetary dissipation rate from satellite tracking estimates of D_{22}^+, ψ_{22}^+.

A set of six recent estimates of D_{22}^+, ψ_{22}^+ for M_2, deduced by several different groups using data from a variety of satellites, has recently been compiled by *Ray et al.* [2001]. After accounting for differences in certain geodetic and astronomical constants and in mathematical formulations used by the different groups, the weighted mean estimates are found to be

$$D_{22}^+ = 3.295 \pm 0.016 \text{ cm} \qquad \psi_{22}^+ = 128.69° \pm 0.28°,$$

implying

$$D_{\text{total}} = 2.536 \pm 0.016 \text{ TW} \quad (4)$$

for the planetary M_2 dissipation rate.

If similar analyses are made for all other lunar tides, including the lunar parts of K_1 and K_2, then the total may be compared with estimates from lunar laser ranging, which accurately measures the Moon's secular acceleration as induced by tidal friction. This has been done [e.g., *Cartwright*, 1993; *Ray*, 1994], and the results are in reasonably good agreement. Note that the lunar ranging measurements cannot establish the rate for M_2 alone, although some progress has been made in separating diurnal from semidiurnal tidal contributions [*Williams et al.*, 1992]. The lunar acceleration is also sensitive to a small, but somewhat uncertain, contribution from tidal friction in the Moon itself [*Williams et al.*, 2001].

2.2. Partition Among Solid and Fluid Tides

As has been known for decades, "most" of the 2.54 TW of the M_2 tide is dissipated in the oceans [*Munk and MacDonald*, 1960], but establishing an exact solid/fluid partition (accurate to the ± 0.016 TW uncertainty of the total) is not yet possible. Let us consider each of the major nonoceanic components.

The M_2 atmospheric tide dissipates about 10 GW = 0.01 TW, according to *Platzman* [1991]. This estimate is based on observational data, namely, surface barometer measurements at 104 meteorological stations, which were gridded and subjected to spherical harmonic analysis by *Haurwitz and Cowley* [1969]. A similar estimate, relying exclusively on numerical simulations, was made by *Kagan and Shkutova* [1985], who arrive at 17 GW. Evidently, the atmosphere accounts for less than 1% of the M_2 planetary dissipation rate.

Dissipation by the Earth's body tide (i.e., the part of the solid tide forced only by the astronomical potential) has been estimated in various ways by a number of authors. *Platzman* [1984] obtained an estimate of 32 GW based on the complex Love number k_2 as calculated by *Zschau* [1978]. But Zschau had employed a solid earth Q appropriate to seismic frequencies. A complex k_2 computed recently by B. Buffett and P. M. Mathews (personal communication, 1999, but cited by *McCarthy* [1996]) assumes a solid Q proportional to ω^α where $\alpha = 0.15$, which appears to be supported by nutation measurements; their $k_2 = 0.3010 - 0.0013\,i$, implying a body tide dissipation of 130 GW. In another approach, *Zschau* [1986] used observations of the Chandler Wobble Q to bound the dissipation to the interval [70, 140] GW with "most probable" value of 120 GW. In yet another approach, *Ray et al.* [1996] combined altimetry and tracking estimates of $D_{22}^+ \sin\psi_{22}^+$ to arrive at a figure recently up-

Table 1. Global Ocean Tide Energy Integrals

Model	D_{22}^{+}, cm	ψ_{22}^{+}, deg	W_{total}, TW
TPXO.4a	3.223 ± 0.017	129.99 ± 0.30	2.435 ± 0.017
TPXO.4b	3.211	129.86	2.430
TPXO.4c	3.229	130.06	2.437
GOT99.0	3.200	129.57	2.432
CSR4.0	3.229	129.41	2.460

dated to 110 ± 25 GW [*Ray et al.*, 2001]. From this evidence it appears safe to conclude that the M_2 body tide dissipation rate is well less than 10% of the planetary rate and probably close to 5%.

Dissipation in the solid earth load tide is more difficult to determine because it depends on all spherical harmonic components of the ocean tide through complex loading numbers k_n' [*Platzman*, 1984]. Platzman concludes that the dissipation is an order of magnitude smaller than the body tide, and we are aware of no evidence to dispute this. Some empirical bounds on the imaginary components of k_n' would be highly desirable.

In summary, a process of elimination suggests that the ocean tide must account for roughly 95% of the M_2 planetary dissipation rate of 2.54 TW. Although it is perhaps not as well determined as one would like, the nonoceanic dissipation is clearly small. In a discussion of local oceanic energy balances, which is our main topic, errors are sufficiently large that consideration of the small nonoceanic component becomes an unnecessary complication. Therefore throughout the remainder of this paper we ignore any nonoceanic components of energy loss and take all Love and loading numbers to be real. Under that assumption the total oceanic dissipation rate, equaling the total rate of working on the ocean by both gravitational and mechanical (solid tide) forces, can be expressed by the same formula (3) given above for the planetary rate [cf. *Hendershott*, 1972; *Cartwright and Ray*, 1991] but with the parameters D_{22}^{+} and ψ_{22}^{+} determined by satellite altimetry. Table 1 lists the global M_2 rate for the primary ocean tide models used extensively below. The quoted uncertainty for the inverse model is based on the error covariances described in section 4; this uncertainty is slightly too small, since it does not account for the small systematic error from assuming k_2 and k_2' are strictly real.

3. Tidal Energy Balance: Theory

This discussion requires a number of different tidal height variables, which are best summarized at the beginning:

- ζ the usual ocean tide height as measured by a tide gauge. It has a spherical harmonic decomposition given by $\zeta = \sum_n \zeta_n$.
- ζ_b the body tide height.
- ζ_l the load tide height.
- ζ_s the solid Earth tide height: $\zeta_s = \zeta_b + \zeta_l$.
- ζ_{EQ} the equilibrium ocean tide height (allowing for the body tide "reduction factor").
- ζ_{SAL} an equilibrium-type tide as induced by self-attraction and loading.

We assume that the barotropic ocean tide satisfies the tidal equations of Laplace, modified to include effects of an elastic Earth and a self-gravitating ocean. Writing these equations in terms of volume transports $\mathbf{U}$ ($= \mathbf{u}H$ where $\mathbf{u}$ is the depth averaged velocity and H is water depth) offers certain advantages. The equations then take the form

$$\frac{\partial \mathbf{U}}{\partial t} + \mathbf{f} \times \mathbf{U} = -gH\nabla(\zeta - \zeta_{\text{EQ}} - \zeta_{\text{SAL}}) - \mathcal{F}, \quad (5)$$

$$\frac{\partial \zeta}{\partial t} = -\nabla \cdot \mathbf{U}, \quad (6)$$

where the gradient and divergence operators are assumed two dimensional, and the Coriolis parameter $\mathbf{f}$ is assumed oriented to the local vertical, g is gravity, and $\mathcal{F}$ is a generic frictional or dissipative stress, including possibly a Reynolds stress through some turbulent viscosity scheme. The equilibrium tides ζ_{EQ} and ζ_{SAL} are given by

$$\zeta_{\text{EQ}} = \gamma_2 \Phi / g$$

$$\zeta_{\text{SAL}} = \sum_n \gamma_n' \alpha_n \zeta_n$$

$$\alpha_n = \frac{3}{2n+1} \frac{\rho}{\rho_e},$$

where $\gamma_2 = (1 + k_2 - h_2)$ and $\gamma_n' = (1 + k_n' - h_n')$ for Love numbers h_2, k_2 and loading numbers h_n', k_n', and where ρ, ρ_e are the mean densities of seawater and Earth, respectively. Aside from the (as yet unspecified) dissipation term, (5) is linear. At least one of the models discussed below employs additional terms in (5)–(6), including advection and turbulent horizontal viscosity, but these features are peripheral to the main discussion of energetics in the open ocean where $\zeta \ll H$ and so are excluded from the equations above.

Equation (5) is sometimes written [*Hendershott*, 1972]

$$\frac{\partial \mathbf{U}}{\partial t} + \mathbf{f} \times \mathbf{U} = -gH\nabla(\zeta + \zeta_s - \Gamma/g) - \mathcal{F}, \quad (7)$$

where Γ is the complete tidal potential, corresponding to both astronomical and induced forcing:

$$\Gamma = (1 + k_2)\Phi + \sum_n (1 + k_n') g \alpha_n \zeta_n.$$

That is, Γ comprises four parts: the astronomical potential Φ, a perturbation $k_2\Phi$ induced by the body tide, a perturbation $\sum k'_n g\alpha_n\zeta_n$ induced by the load displacements and a perturbation $\sum g\alpha_n\zeta_n$ from self-attraction. Equation (7) follows from (5) because

$$\begin{aligned} g(\zeta_{EQ}+\zeta_{SAL}) &= (1+k_2)\Phi + g\sum_n (1+k'_n)\alpha_n\zeta_n - \\ &\quad h_2\Phi - g\sum_n h'_n\alpha_n\zeta_n \\ &= \Gamma - g\zeta_b - g\zeta_l = \Gamma - g\zeta_s. \end{aligned}$$

Notice that $\zeta + \zeta_s$ in (7) is the geocentric (ocean + Earth) tide.

Equations (5) and (6) give expressions for the local balance of momentum and mass. These equations may be combined in any number of different ways to form an energy balance equation that describes the trade-off between terms that may be identified with work, flux, and dissipation at a given location [e.g., *Hendershott*, 1972; *Zahel*, 1980; *Le Provost and Lyard*, 1997]. The different forms of energy balance that are found in the literature reflect omission of supposed secondary terms like tidal loading and self-attraction, and different definitions for work and flux, which do not have an obvious form when allowance is made for a nonrigid Earth. Of course, all correct balance equations must arrive at equivalent dissipations.

A derivation of an energy balance equation from first principles was given by *Taylor* [1919], who wrote down expressions for potential and kinetic energy in a fixed Eulerian volume of ocean and then used the principal of energy conservation to derive the balance between work done by body forces and forces acting on the boundary, advection of energy into the volume, and dissipation. In the next section we use a similar approach to clarify the proper definition of work and flux terms on a nonrigid Earth. After dropping small terms, consistent with the approximations leading to (5) and (6), equations identical to those given by *Hendershott* [1972, 1977] are obtained. Because several of the terms take an unfamiliar form (and because of some typographical errors in the original papers), it is worth considering this derivation in further detail.

3.1. Potential Energy and Flux on an Elastic Earth

The following discussion briefly repeats the analysis of *Taylor* [1919] for potential energy and energy fluxes, but allowing for elastic tidal deformations of the Earth.

The usual expression for the potential energy density is derived by integrating $\rho g z$ over the water column [e.g., *Gill*, 1982, p. 80]. When the seabed is also moving vertically, $\zeta_s = \zeta_b + \zeta_l$ must be added to z to account for the additional potential energy associated with vertical displacement of the entire water column. Following Taylor, we thus take the extended potential energy density to be

$$\mathrm{PE} = \rho g\int_{-H}^{\zeta}(z+\zeta_s)\,dz = \tfrac{1}{2}\rho g(\zeta^2 - H^2 + 2\zeta\zeta_s + 2H\zeta_s). \tag{8}$$

After subtracting the rest state potential energy $-\frac{1}{2}\rho g H^2$, the mean potential energy density over a tidal cycle is

$$\langle \mathrm{PE}\rangle = \tfrac{1}{2}\rho g\left(\left\langle\zeta^2\right\rangle + \langle 2\zeta\zeta_s\rangle\right). \tag{9}$$

This expression agrees with *Hendershott* [1972].

Consider now the vertically integrated time-averaged energy flux $\mathbf{P}$ at a point where the tidal current velocity is $\mathbf{u}$. Again following Taylor, the energy flux across a fixed (Eulerian) surface $\mathcal{S}$ bounding a column of water is the sum of the work done on the water mass by the hydrostatic pressure p of the surrounding ocean, and the energy (potential (PE) and kinetic (KE)) advected into the volume

$$\begin{aligned} \int_{\mathcal{S}} \mathbf{P}\cdot\hat{\mathbf{n}}\,dl &= \int_{\mathcal{S}}\int_{-H}^{\zeta}\langle p\mathbf{u}\rangle\cdot\hat{\mathbf{n}}\,dz\,dl + \\ &\quad \int_{\mathcal{S}}\langle(\mathrm{PE}+\mathrm{KE})\mathbf{u}\rangle\cdot\hat{\mathbf{n}}\,dl. \end{aligned} \tag{10}$$

In (10) $\hat{\mathbf{n}}$ is the outward directed normal to the surface $\mathcal{S}$, and PE and KE are vertically integrated potential and kinetic energy densities. The advected kinetic energy term can be neglected because it involves third powers in the current velocity [*Taylor*, 1919]. The mean pressure throughout the water column is $\frac{1}{2}\rho g(H+\zeta)$, so the first term on the right side of (10) is $\frac{1}{2}\rho g(H+\zeta)^2\mathbf{u}\cdot\hat{\mathbf{n}}$. Combining this with the potential energy from (8), the mean energy flux is

$$\begin{aligned} \mathbf{P} &= \rho g\left\langle\mathbf{u}\left(\zeta^2 + \zeta H + \zeta\zeta_s + \zeta_s H\right)\right\rangle \\ &\approx \rho g\,\langle\mathbf{U}(\zeta+\zeta_s)\rangle, \end{aligned} \tag{11}$$

assuming, as usual, that $H \gg \zeta$. This too agrees with Hendershott. The flux $\mathbf{P}$ computed using (11) is plotted below in Figure 1.

3.2. Energy Balance Equation

Equations (6) and (7) are readily combined to form a mean energy balance of the form [*Hendershott*, 1972, 1977]

$$\underset{W}{\text{Gravitational work}} - \underset{F}{\text{Bottom flux}} - \underset{\nabla\cdot\mathbf{P}}{\text{Horizontal flux}} = \underset{D}{\text{Dissipation}}. \tag{12}$$

An expression for $\mathbf{P}$ is given in (11). The mean rate of working of tidal gravitational forces (including the self-attraction forces) is

$$W = \rho\,\langle\mathbf{U}\cdot\nabla\Gamma\rangle \tag{13}$$

$$= \rho\nabla\cdot\langle\Gamma\mathbf{U}\rangle + \rho\,\langle\Gamma\partial\zeta/\partial t\rangle, \tag{14}$$

the last line from substituting (6). The term $-F$ represents mechanical working by the solid tide against the ocean, or equivalently [*Platzman*, 1985] F is a flux of energy from the ocean into the solid Earth. This flux is given by the pressure fluctuation $\rho g\zeta$ times the downward velocity of the ocean-solid interface

$$F = -\langle\rho g\zeta\,\partial\zeta_s/\partial t\rangle = \langle\rho g\zeta_s\,\partial\zeta/\partial t\rangle. \tag{15}$$

Note that our use of F and W follows *Platzman* [1985] (ex-

cept that his variables denote global integrals); our $(W - F)$ is equivalent to the $\langle W_t \rangle$ of *Hendershott* [1972]; and the global integral of our $(W - F)$ is equivalent to the W of *Cartwright and Ray* [1991].

The work terms in (12) can be decomposed as $W = W_a + W_b$ and $F = F_a + F_b$, where

$$W_a = \rho \langle \mathbf{U} \cdot \nabla (1 + k_2) \Phi \rangle \quad (16)$$

$$W_b = \rho \langle \mathbf{U} \cdot \nabla \textstyle\sum_n (1 + k_n') g \alpha_n \zeta_n \rangle \quad (17)$$

$$F_a = \rho g \langle \zeta_b \, \partial \zeta / \partial t \rangle \quad (18)$$

$$F_b = \rho g \langle \zeta_l \, \partial \zeta / \partial t \rangle . \quad (19)$$

Thus W_a and F_a arise from the large-scale astronomical potential and body tide, while W_b and F_b arise from the loading and self-attraction effects. These terms are individually evaluated and plotted below in Plate 1.

In principle, evaluation of the quantities W, F, and $\mathbf{P}$ in (12) provides a method for mapping the dissipation D throughout the ocean, regardless of the physical mechanism of that dissipation. The complications arise from the unavoidable errors in estimating these quantities, which depend on tidal volume transports throughout the ocean.

3.3. Energy Balance Over Patches

One can anticipate that the spatial resolution of dissipation estimates derived from T/P tidal elevations will be limited, both by noise and by the incomplete data coverage. However, the integral of D over a large ocean patch might be reliably estimated even when the small-scale details of D in the same area are poorly determined. There are several ways in which these patch integrals can be calculated, and some care is warranted. To make this explicit, let an overbar denote area integration, so that the dissipation in some closed region is given by $\overline{D} = \overline{W} - \overline{F} - \overline{\nabla \cdot \mathbf{P}}$. By expressing W via (14), rather than as $\rho \langle \mathbf{U} \cdot \nabla \Gamma \rangle$, all terms in $\overline{D}$ involving $\mathbf{U}$ are surface integrals of divergences, and may thus be replaced by line integrals in which knowledge of $\mathbf{U}$ is required only along open boundaries of the patch. These boundaries may be conveniently placed to avoid shallow seas and regions of complex topography where the currents are more likely to be poorly determined.

Substituting explicit expressions from (11), (14), and (15), and simplifying yields

$$\overline{D} = \rho g \iint \langle (\zeta_{EQ} + \zeta_{SAL}) \, \partial \zeta / \partial t \rangle \, dS - \rho g \int \langle (\zeta - \zeta_{EQ} - \zeta_{SAL}) \, \mathbf{U} \cdot \hat{\mathbf{n}} \rangle \, d\ell, \quad (20)$$

where $\hat{\mathbf{n}}$ is a unit vector directed normal to the open boundary and away from the region of interest. These integrals may be interpreted as a direct work integral minus a boundary flux integral (although the terms do not correspond to our W and $\mathbf{P}$). The flux-like integral includes the so-called equilibrium flux of *Garrett* [1975], extended to include the self-attraction and loading effects. Garrett points out that *Taylor* [1919], and many others since Taylor, left out the ζ_{EQ} term from the flux; some authors continue to do so, but at least in Taylor's case it was probably permissible because in the Irish Sea is much greater than the equilibrium tide.

3.4. Energy Balance Over the Globe

As is well known [*Hendershott*, 1972; *Platzman*, 1985], further simplification of the balance equation occurs when the spatial integration is taken over the entire globe. All divergence terms of form $\nabla \cdot (\mathbf{U}X)$, when integrated to impermeable coasts, drop out. In addition, all terms involving k_n' or h_n' drop out because they lead to factors of the form $\langle \zeta_n \, \partial \zeta_n / \partial t \rangle = 0$. We are left with

$$\overline{D} = \rho g \iint_{\text{globe}} \langle \zeta_{EQ} \, (\partial \zeta / \partial t) \rangle \, dS. \quad (21)$$

Of all the surface harmonics $\sum_n \zeta_n$ forming ζ, only the $n = 2$ term in quadrature with the equilibrium tide ζ_{EQ} contributes to this integral. The result, along with the Saito-Molodensky relation $k_2' = k_2 - h_2$, leads directly back to (3).

4. Estimates of Tidal Volume Transports

4.1. General Considerations

To map barotropic tidal energy dissipation using (11)–(15), we require the ocean and solid Earth tidal elevations ζ and ζ_s, the complete tidal potential Γ, and volume transports $\mathbf{U}$. T/P altimetry data provide direct constraints on the elevations, and a number of nearly global maps of ζ are now available. Given ζ, calculation of the tidal loading and self-attraction parts of Γ and ζ_s are straightforward [*Ray*, 1998]. The primary challenge is estimation of the volume transports $\mathbf{U}$ in the open ocean.

With elevations already specified (from the altimetry data) the momentum equations essentially involve two unknown fields: $\mathbf{U}$ and $\mathcal{F}$. Given $\mathcal{F}$, or strong enough assumptions about this dissipation term, it would be straightforward to directly solve for $\mathbf{U}$. For example, assuming that

$$\mathcal{F} = r \mathbf{U} / H, \quad (22)$$

with the linear drag coefficient r known, volume transports can be estimated by substituting ζ into (5) and solving the resulting 2×2 linear system for $\mathbf{U}$ at each point in the domain. This is the approach (with $r = 0$) used by *Cartwright and Ray* [1989] in their estimate of dissipation on the Patagonian shelf from Geosat altimeter data. This simple approach requires only a local calculation and is thus easily implemented, but the explicit assumptions about energy dissipation required might be expected to bias estimates of dissipation computed from the resulting $\mathbf{U}$.

More importantly, this simple approach completely ignores the continuity equation, so the estimated volume transports will not in general conserve mass [e.g., *Cartwright et al.*, 1980]. In fact, (6) provides a powerful constraint on $\mathbf{U}$, independent of any assumptions about dissipation. It effectively provides the additional equations needed to extract meaningful information about both $\mathcal{F}$ and $\mathbf{U}$ from knowledge of ζ and hence to map dissipation. Enforcing (6) also leads to smoother estimates of volume transports which are less affected by noise in the tidal elevation fields. As we

shall show below, estimates of dissipation computed without explicitly enforcing mass conservation are too noisy to be useful.

Our strategy is to estimate the currents by fitting both (5) and (6) in a least squares sense. Since (6) is a simple statement of mass conservation that does not depend on any unknown parameters, fit to this equation should be emphasized. Based on comparison of a number of global tidal solutions to pelagic and island tide gauges, *Shum et al.* [1997] estimate errors in T/P constrained open ocean elevation fields to be of the order of 1 cm or so. Fit to (6) should be consistent with this level of accuracy. If misfit to the continuity equation is significantly larger in the open ocean, the estimated transports are not truly consistent with the altimetrically constrained elevations. On the other hand, the momentum conservation equations (5) entail several approximations and depend on imperfectly known bathymetry as well as the dissipative term $\mathcal{F}$. Most of the misfit between the dynamics and the altimeter data should thus be accommodated by these equations.

The least squares fitting approach still requires us to make a priori assumptions about dissipation in order to complete the definition of the momentum equations. To verify that these assumptions do not unduly influence the results we use a large suite of tidal elevation models (both T/P and synthetic) with a wide range of assumptions about $\mathcal{F}$. We also use two distinct approaches for estimating U: the variational data assimilation scheme of *Egbert et al.* [1994] (hereinafter referred to as EBF) and a scheme based on least squares fitting of the shallow water equations to gridded tidal elevation fields [*Ray*, 2001]. For completeness and to facilitate subsequent discussion, we briefly summarize the two methods here.

4.2. Data Assimilation

By assimilating the T/P altimetry data into the shallow water equations, tidal elevation and volume transport fields can be estimated simultaneously. For this study, new M_2 tidal solutions have been computed using a refinement of the variational assimilation scheme described in EBF [see *Egbert and Bennett*, 1996; *Egbert*, 1997; *Egbert and Erofeeva*, 2001]. Briefly, the method requires minimizing a quadratic penalty functional formally expressed as

$$\mathcal{J}[\mathbf{w}] = (\mathbf{Lw}-\mathbf{d})^{*}\boldsymbol{\Sigma}_{\mathbf{e}}^{-1}(\mathbf{Lw}-\mathbf{d}) + (\mathbf{Sw}-\mathbf{a})^{*}\boldsymbol{\Sigma}_{\mathbf{f}}^{-1}(\mathbf{Sw}-\mathbf{a}), \quad (23)$$

where $\mathbf{w}$ represents the tidal fields (ζ and $\mathbf{U}$), $\mathbf{S}$ represents the shallow water equations (including boundary conditions), $\mathbf{a}$ represents the forcing, and $\mathbf{d} = \mathbf{Lw} + \epsilon_d$ represents the altimetry data. $\boldsymbol{\Sigma}_{\mathbf{e}}$ and $\boldsymbol{\Sigma}_{\mathbf{f}}$ are covariances which express a priori beliefs about the magnitude and correlation structure of errors in the data (ϵ_d) and the assumed dynamical equations, respectively. As in EBF we assume a nonlocal dynamical error covariance $\boldsymbol{\Sigma}_{\mathbf{f}}$ with spatially varying amplitudes, and a globally constant decorrelation length scale, generally 5 degrees. The continuity equation (6) is assumed exact, since the assimilation approach estimates the elevations and volume transports simultaneously and already allows for misfit between the estimated ζ and the altimetry data.

To allow for nonlinearity in the shallow water equations, (23) is minimized with a two-step procedure. In the first step a prior model is calculated by time stepping a finite difference approximation to the nonlinear shallow water equations on a $\frac{1}{4}^{\circ}$ nearly global (80°S–80°N) grid. At the northern limit, elevations derived from the FES94.1 model of *LeProvost et al.* [1994] are used for boundary conditions. The forcing includes the four dominant constituents, M_2, S_2, K_1, O_1, with tidal loading and ocean self-attraction (i.e., ζ_{SAL} in (5)) calculated as described by *Ray* [1998] using elevations from the TPXO.3 global solution of *Egbert* [1997]. Bottom friction is assumed to be quadratic in velocity

$$\mathcal{F} = c_D \mathbf{U} v / H, \quad (24)$$

where v is the total water speed (including all tidal constituents), and the nondimensional parameter $c_D = 0.003$. Advection, the nonlinear term in the continuity equation, and a horizontal eddy viscosity term $HA_h\nabla^2\mathbf{u}$, with $A_h = 10^3\ \mathrm{m^2\ s^{-1}}$ are also included in the prior model calculation, although the effect of these additional terms appears to be minimal. In the second step we linearize the dissipation using the spatially varying velocities from the prior solution, omit other nonlinear terms from the shallow water equations, and use the reduced basis representer approach of EBF to approximately minimize (23). See EBF and *Egbert and Erofeeva* [2001] for further details on the computational approach.

For the inverse solutions described here we fit T/P data for 232 orbit cycles, including data from all crossover points and one point between each crossover. Because of computational limitations the final inverse solution was computed on a $\frac{3}{4}^{\circ}$ grid, instead of the $\frac{1}{4}^{\circ}$ grid used for the purely hydrodynamic prior model. To assess the sensitivity of dissipation estimates to assumptions about the dynamical errors, inverse solutions are computed with three different assumed forms for $\boldsymbol{\Sigma}_{\mathbf{f}}$. In the following we refer to these inverse solutions as TPXO4a, b, and c. Further details on the error covariances used are given in EBF and in section 5.3.

The assimilation approach allows us to calculate formal error bars on the tidal fields and on the estimates of tidal energy flux and dissipation. These error bars of course depend on the assumed a priori error structure (i.e., $\boldsymbol{\Sigma}_{\mathbf{f}}$) and should be interpreted in conjunction with other measures of solution stability and validation data. The posterior errors for the inverse solutions are computed by a Monte Carlo method. First, a realization of the random forcing error is generated with covariance $\boldsymbol{\Sigma}_{\mathbf{f}}$. The corresponding error in the tidal model $\delta\mathbf{w}_i$ is then found by solving the linearized shallow water equations. The realization of the random tidal fields is then given by $\mathbf{w}_i = \mathbf{w}_0 + \delta\mathbf{w}_i$, where $\mathbf{w}_0$ is the same prior model used for the inverse solution (i.e., the solution to the astronomically forced nonlinear shallow water equations). The solution is sampled with the spatial and temporal pattern of the altimeter, random data errors are added, and the

resulting synthetic data vector is inverted for $\hat{\mathbf{w}}_i$. The difference $\mathbf{w}_i - \hat{\mathbf{w}}_i$ is then a realization of the error in the estimated tidal fields. If a number of realizations $\mathbf{w}_i$, $i = 1, \ldots, I$ are calculated, actual and estimated dissipation maps D_i, $\hat{D}_i$ can be computed for each of $\mathbf{w}_i$ and $\hat{\mathbf{w}}_i$, and error bars for D (or area integrals of D) can be calculated. By adjusting the scale of the assumed dynamical error covariance $\Sigma_\mathbf{f}$ we can ensure that the dynamical residuals for the synthetic tidal fields used in the error calculation have amplitudes and spatial structure consistent with the actual dynamical residuals required to fit the data. Further details on the posterior error calculation are given by *Dushaw et al.* [1997] and *Egbert and Erofeeva* [2001].

4.3. Least Squares Inversion of Elevation Solutions for Volume Transports

Using the weighted least squares procedure described by *Ray* [2001], volume transports, and hence estimates of energy dissipation, can be computed from any of the global T/P tidal elevation solutions. Given a gridded tidal elevation field ζ, $\mathbf{U}$ is estimated by minimizing the weighted misfit to the equations (5)-(6),

$$\mathcal{M}_\mathbf{U}[\mathbf{U}, \zeta] + w_\zeta \mathcal{M}_\zeta[\mathbf{U}, \zeta]. \tag{25}$$

Here $\mathcal{M}_\mathbf{U}$ and $\mathcal{M}_\zeta$ give the squared misfits to the two equations, and the weight w_ζ controls the relative degree of fit to each equation. In the limit of large w_ζ, continuity is enforced exactly, while in the limit of small w_ζ the momentum equations will be satisfied exactly. As *Ray* [2001] shows, in the open ocean currents estimated by solving this large least squares problem are quite similar to those obtained by the assimilation method discussed above and show good agreement with reciprocal acoustic tomography and current meter data. Further details, including treatment of coastal boundary conditions and computational procedures are given by *Ray* [2001].

In addition to w_ζ, the least squares solution will depend on the assumed form for the bottom drag term in the momentum equations. To keep the least squares problem linear, the linear parameterization of bottom drag (22) is used in (5), with r varied over a wide range.

5. Results

Both the data assimilation and the least squares procedures result in elevation and volume transport fields which can be substituted into (11)–(19) to yield estimates of time-averaged fluxes, work terms, and dissipation. Some numerical details of these calculations are given in the Appendix. E-R presented dissipation maps derived in this way for two different tidal solutions: GOT99, an empirical correction by *Ray* [1999] to the FES95.2 solution of *Le Provost et al.* [1998], with currents computed using the weighted least squares approach of section 4.3, and the TPXO.4 inverse solution described in section 4.2. Based on these maps, E-R concluded that about 25-30% of the M_2 tidal dissipation occurred in the open ocean, mostly in areas of rough bottom topography. Here we consider these results in much greater detail, and we demonstrate the robustness of these empirical dissipation estimates to details in the T/P tidal solutions, prior dynamical assumptions and weightings, and errors in bathymetry.

5.1. Energy Fluxes and Rates of Working

We begin with a brief examination of the individual terms in the energy balance equation (12). As these are almost indistinguishable for the full range of solutions considered, results are shown for only TPXO.4a. The mean barotropic energy flux for the M_2 constituent is shown in Figure 1. These fluxes immediately suggest that certain shallow seas are important energy sinks. Large fluxes are observed entering the European shelf, the Norwegian, Greenland, and Labrador Seas, the Yellow, East China, and Timor Seas, and the Patagonian Shelf. The very substantial flux of energy passing from the South Atlantic into the North Atlantic is astonishing, amounting to 420 GW (although this is about 200 GW less than the hydrodynamic estimate of *Le Provost and Lyard* [1997], even after accounting for differences in the definition of flux). Other features to note include the

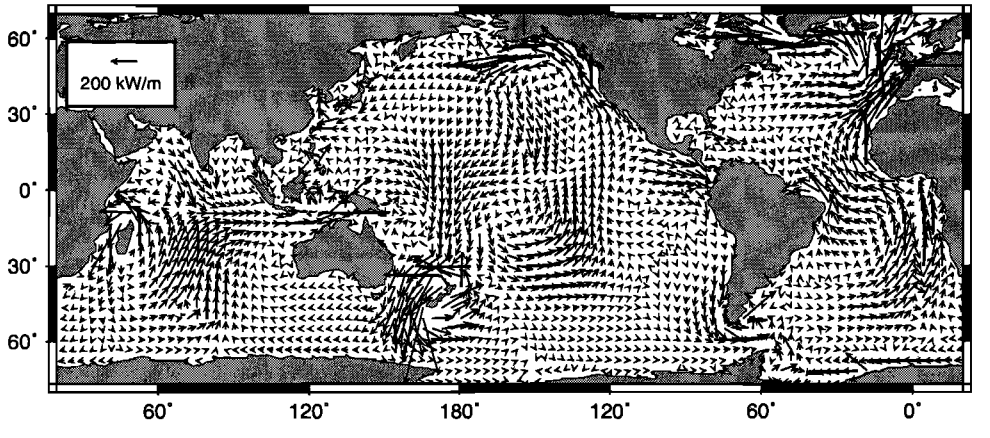

Figure 1. Energy flux vectors $\mathbf{P}$ for M_2 derived using elevations and currents from the assimilation solution TPXO.4a.

pronounced counterclockwise flux of energy around New Zealand, and the flux paralleling the west coast of North America. The pattern of energy flux inferred from the T/P data is generally similar to that obtained by *Le Provost and Lyard* [1997] from the finite element hydrodynamic solution FES94.1.

Plate 1 shows the cycle averages of the work terms W_a, W_b, $-F_a$, and $-F_b$ defined in (16)–(19), their sum, and the energy flux divergence $\nabla \cdot \mathbf{P}$. Note the difference in color scales: the terms associated with the large-scale potential and body tides (W_a and $-F_a$) are an order of magnitude larger than the terms associated with loading and self attraction (W_b and $-F_b$). W_a (the work done by the body forces associated with the large-scale potential) is large only in the deep open ocean where volume transports are significant. It is generally positive, with large areas of energy input in the South Atlantic and Southwest Indian Oceans, but there are also areas where the ocean locally does work on the Moon (and the solid Earth). The global integral of W_a for TPXO.4a is 4.566 TW.

The work term associated with the body tide ($-F_a$) has a magnitude comparable to W_a but a very different appearance. There is significant work done by the ocean on the solid Earth in a series of large (blue) spots around the equator. At midlatitudes the situation is reversed, with a tendency for the body tide to do work on the oceans. The body tide also does significant work on the ocean around Australia and in the north Indian Ocean. F_a nearly balances the part of W_a due to work by the body tide gravitational potential on the ocean. In contrast to W_a, F_a is not obviously affected by the bathymetry (e.g., note the smoothness of this term) and can be quite large in shallow water.

The loading and self-attraction terms W_b and $-F_b$ have smaller amplitude and tend to be dominated by smaller scale features (especially W_b). Although W_b is also integrated over the water column and obviously affected by bathymetry, it is still large in some shallow seas where large tidal elevations and short spatial scales can result in large amplitudes for the gradients of $\sum_n (1 + k'_n) g \alpha_n \zeta_n$. For example, note the large amplitude of W_b on the European, North Australian, and Patagonian shelves, and near the Gulf of Maine on the east coast of North America. The work done by the load tide on the ocean ($-F_b$) is the smallest of the terms considered. Magnitudes peak in shallow seas and along the edges of continents. The global integrals of W_b and F_b are 0.009 and −0.001 TW, respectively. The two terms should in principle integrate to zero globally, since we have assumed real Love numbers. The small discrepancies arise from several sources: (1) combining loading and self-attraction calculated from TPXO.3 tidal elevations with tidal elevations and currents from a different inverse tidal solution, TPXO.4, (2) nonvanishing of currents on the coastal boundaries in TPXO.4a, and (3) incomplete global coverage of the tidal solution. These factors also lead to small discrepancies between the global totals for work (Table 1) and dissipation (Table 2) for each of the solutions.

The most striking aspect of Plate 1 is the almost identical appearance of the net work done on the ocean by all body forces and the moving seafloor ($W - F$) and the divergence of the energy flux $\nabla \cdot \mathbf{P}$. Thus, for example, most of the energy input to the ocean in areas of positive net work (red areas in Plate 1e) propagates away as barotropic waves. Plate 1 underscores the difficulty of estimating dissipation, which is the difference between the two very similar terms $D = (W - F) - \nabla \cdot \mathbf{P}$. Evidently, great care must be exercised in all phases of these calculations. In particular, although tidal loading and self attraction are small compared with the total work $W - F$, they cannot be neglected and, in fact, must be calculated as accurately as possible.

5.2. Localized Dissipation Estimates

Before discussing dissipation maps estimated from the T/P data, we briefly consider dissipation in the purely hydrodynamic prior solution used as the prior or first guess for all of the assimilation solutions. The prior was computed by time stepping the nonlinear shallow water equations on a $\frac{1}{4}^\circ$ grid, and then averaging the elevations ζ_0 and transports $\mathbf{U}_0$ onto the $\frac{3}{4}^\circ$ grid used for assimilation of the T/P data. Dissipation was then estimated using (11)–(15). The result is plotted in Plate 2a. Note the occurrence of both negative (blue) and positive (red) dissipation. Negative dissipation is, of course, physically implausible and is indicative of the level of noise in the empirical dissipation maps. Consistent with the parameterization of bottom drag with the quadratic law of (24), for which dissipation is cubic in current speed, significant energy sinks in the prior solution are restricted to shallow seas and broad continental shelves where tidal velocities are greatest.

In addition to showing where dissipation by bottom drag is expected to be large, Plate 2a illustrates some of the artifacts that can contaminate empirical dissipation maps. The plot has a slightly noisy appearance with numerous small spots of negative and positive dissipation in the open ocean (e.g., in the North Atlantic, the western Pacific around New Zealand, the western Indian Ocean near Madagascar, around the Hawaiian Islands, and the Kerguelan Plateau). Noise in Plate 2a (which is derived from a purely numerical model) results primarily from averaging of the $\frac{1}{4}^\circ$ solution onto a coarser grid in which some bathymetric details are no longer resolved. Other contributing factors include the inexact cancellation in the energy equation of the Coriolis terms on the C grid and noise in the loading and self attraction terms due to truncation of the spherical harmonic expansion used for their computation. In general, the small blue spots of negative dissipation occur in tandem with red spots of positive dissipation. The clearest example is provided by the Hawaiian Ridge, which appears red on the north side and blue on the south. The Azores, and Canary and Cape Verde Islands in the eastern north Atlantic, Somoa and Fiji in the south Pacific, the Galapagos Islands, and the Mascerene Islands in the Indian Ocean have a similar appearance. Comparison with Figure 1 reveals that in all cases the blue patches occur on the "downstream" side of the unresolved islands, relative to the direction of tidal energy flux. These features result primarily from residuals in the dynamical equations

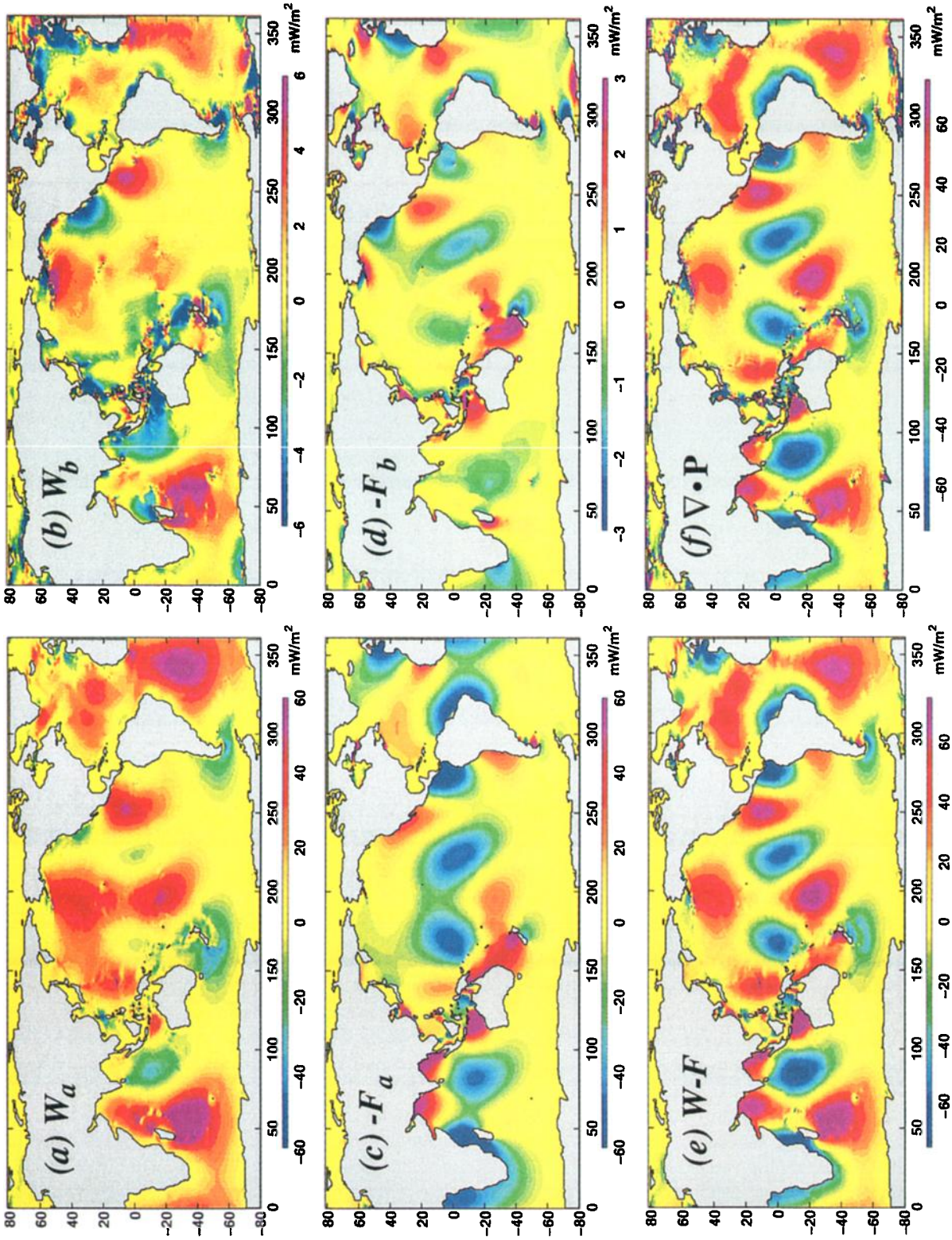
(a) W_a
(b) W_b
(c) $-F_a$
(d) $-F_b$
(e) W-F
(f) $\nabla \cdot \mathbf{P}$
mW/m^2

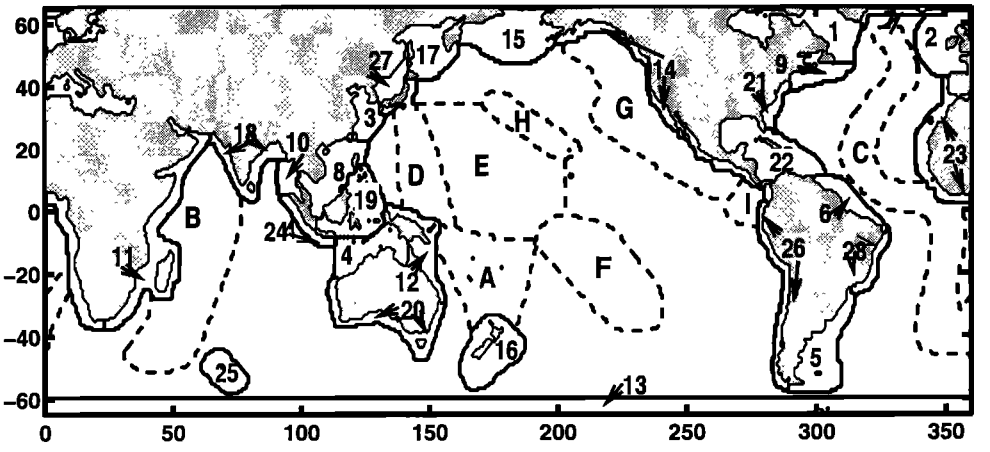

Figure 2. Shallow seas and deep ocean areas used for integrated dissipation computations. Areas outlined with solid lines, numbered 1-28, include all of the shallow seas where significant dissipation due to bottom boundary layer drag would be expected. In particular, essentially all of the dissipation in the prior model (Plate 2a) occurs within these areas. Areas outlined with dashed lines and labeled A-I are deep-water areas which show enhanced dissipation in the T/P estimates of Plate 2.

which simulate the interaction of the barotropic tide with topographic features present in the fine grid but not resolved by the coarser grid. The pairing of red and blue spots around this unresolved topography implies that these residuals on average do no net work around any particular feature. We demonstrate this more explicitly below by computing area integrals of dissipation for the prior solution. Because the real ocean has topography that will not be resolved in the dynamical equations used to estimate currents, we should expect similar sorts of noise (and areas of negative dissipation) in all of our estimates of D.

The remaining three panels of Plate 2 show dissipation maps based on three tidal solutions representative of the different approaches used to estimate tides from T/P data: formal assimilation methods, empirical corrections to a hydrodynamic model, and purely empirical solutions. The first two of these maps (Plates 2b and 2c) are the TPXO.4a and GOT99hf estimates presented in E-R. The third approach, a purely empirical solution with no explicit reliance on any dynamical assumptions, is represented by the DW95 solution of *Desai and Wahr* [1995] (Plate 2d). For the GOT99hf and DW95 solutions, volume transports were computed using the least squares approach of section 4.2, with the linear friction parameter of (22) set to a relatively high value ($r = 0.03$), and the weight w_ζ of (25) chosen so that $-\nabla \cdot \mathbf{U}/i\omega$ agrees with the tidal elevation ζ to within about 1 cm over most of the open ocean [*Ray*, 2001].

The dissipation map from TPXO.4a has the cleanest appearance, while the map from the purely empirical DW95 solution is noisiest, with significant areas of negative dissipation throughout the ocean. However, all three maps have many features in common. The areas of intense dissipation expected due to bottom boundary layer drag in the shallow seas (e.g., Patagonian Shelf, Yellow Sea, northwest Australian Shelf, European Shelf) are clearly evident in all cases (compare to the prior solution of Plate 2a). The areas of enhanced open ocean dissipation discussed in E-R are also seen in maps for all three T/P-constrained solutions (but not for the prior solution). For example, dissipation is clearly enhanced in the Pacific over the Hawaiian Ridge, the Tuamotu archipelago, and over the back arc island chains extending from Japan southward to New Zealand. The western Indian Ocean around the Mascerene Ridge and south of Madagascar also exhibits enhanced dissipation in all three of the maps. The Mid-Atlantic Ridge shows up most clearly in the assimilation estimate but is evident also in the other two estimates. In all three cases there is substantial dissipation throughout much of the North Atlantic. All of these areas where dissipation is consistently enhanced are characterized by significant bathymetric variation, generally with

Plate 1. Terms in the time averaged energy balance equation (12), derived from the assimilation solution TPXO.4a. In Plates 1a through 1d the work terms are subdivided as in (16)-(19). (a) The work done on the ocean by the large-scale gravitational potential, and (b) the work done by potential terms associated with loading and self-attraction. (c) and (d) Work done by the moving bottom on the ocean, associated with the body tide ζ_b, and load tide ζ_l, respectively. (e) The sum of the four work terms plotted in Plates 1a through 1d, and (f) the divergence of the energy flux $\nabla \cdot \mathbf{P}$. Note that Plates 1e and 1f nearly cancel; the difference is used to estimate the oceanic tidal energy dissipation rate.

elongated features such as ridges and island chains oriented perpendicular to tidal flows.

Dissipation maps computed for other T/P-constrained tidal solutions are grossly similar. Rather than plot all of these maps, we compute integrals of D over discrete patches of ocean to compare more quantitatively the large-scale patterns of dissipation. E-R presented estimates of M_2 tidal dissipation for major shallow sea sinks and selected deep ocean areas for TPXO.4a, GOT99hf, and several variants on these solutions which we consider in greater detail in the next section: TPXO.4b,c (computed with a different dynamical error covariance Σ_f) and GOT99nf (based on currents estimated with "no friction," i.e., $r = 0$). Here we present more complete results for a larger set of tidal solutions, including integrated dissipation estimates for all shallow seas and continental shelves. These are divided into 28 areas with boundaries indicated by the solid lines in Figure 2. The areas chosen roughly follow the compilation of *Miller* [1966], though we have merged some adjacent small or low dissipation shelf areas (e.g., the narrow shelf along the west coast of North America is treated as one area for our computations). We also compute the area-integrated dissipation for 11 open ocean patches, outlined by dashed lines and labeled A–I in Figure 2. These have been chosen to correspond to the general areas of enhanced dissipation seen in Plate 2. In contrast to the shallow seas, none of these areas should contribute significantly to dissipation by bottom drag (see Plate 2a).

Tidal currents are unlikely to be well constrained by altimeter data in shallow seas or in areas with small islands or other topographic complications. However, by computing the dissipation integrals using (20) we require volume transports only on the open ocean boundaries. By drawing these boundaries in deep water and avoiding areas of complex topography, reasonable estimates of dissipation can be computed even for shallow seas. This is also the approach used by *Miller* [1966], who relied on a very sparse and only partly reliable set of tidal elevation and current observations in his estimates of shallow seas dissipation.

Results are given in Table 2 and Plate 3 for the five solutions considered by E-R (TPXO.4a,b,c, GOT99hf,nf), for TPXO.3 (an older version of the inverse solution, described by *Egbert* [1997]), and for a selection of additional tidal solutions derived from T/P altimeter data: DW95, CSR3.0, SR96, and FES95.2. For all of these additional solutions (which are summarized by *Shum et al.* [1997]), volume transports were computed using the least squares scheme with $r = 0.03$, and w_ζ chosen to emphasize fit to the continuity equation. Table 2 also gives the area-integrated dissipation computed for the regridded prior model of Plate 2a, and error bars for the TPXO.4a solution, computed using the Monte Carlo procedure outlined above. For comparison we also include two previously published estimates of shallow sea dissipation in Table 2; these will be discussed in section 6.

For all of the T/P estimates the dominant sinks of energy are in a small number of shallow seas and broad continental shelves. The largest (greater than about 100 GW each) are around Hudson Bay (including the Labrador Sea, Baffin Bay, and Canadian Arctic straits), the European shelf (including the North Sea), the Yellow and East China Seas, the northwest coast of Australia, the Patagonian shelf, and the northeast coast of Brazil in the area around the Amazon Cone. Other shallow seas with significant dissipation (greater than about 50 GW each) include the South China Sea, the St. Lawrence Seaway and Gulf of Maine (including the Bay of Fundy), the Andaman Sea, East Africa (including the Mozambique Channel), New Guinea and northeastern Australia, and Antarctica. The dissipation in the Arctic Ocean and Norwegian Sea is also significant (together nearly 100 GW), but because the T/P data do not extend beyond 66°N latitude, we do not attempt to divide dissipation between these seas. The total, which is determined primarily by the energy flux out of the northeast Atlantic (in an area of good T/P data coverage), is similar for all of the T/P solutions and thus appears to be reasonably well constrained.

For almost all of these major shallow sea sinks the TPXO and GOT99 dissipation estimates (red and blue symbols in Plate 3) agree within approximately 10-15%. Better agreement is obtained for isolated shallow seas that can be cleanly separated from other possible sinks (e.g., the Patagonian Shelf (5), the St. Lawrence Seaway/Gulf of Maine (9), and the Bering and Okhotsk Seas (15) and (17)). Note that for these areas the error bars computed for the TPXO.4a solution are small. Dissipation estimates based on the other T/P solutions (green symbols in Plate 3) show more scatter, but except for a few outliers most estimates are still within about 20% of the average. It should be noted that these other tidal solutions are based on much less T/P data and are generally of lower quality than the more recent TPXO and GOT99 solutions [e.g., *Ray*, 1999]. There is also generally excellent agreement among all solutions in areas of minimal dissipation (e.g., the west coast of South America, the east coast of North America (south of the Gulf of Maine), the west coast of Africa, and the coast of Australia (excluding the northwest coast and Coral Sea).

The area of greatest disagreement between solutions is around Indonesia. Division of dissipation between the various patches in these areas is problematic, since boundaries must be drawn in shallow areas with complex bathymetry where our estimates of volume transports are most questionable. Agreement between all estimates is much better for the total dissipation in the three areas which share boundaries in this area of complex topography (4, 8 and 19, the northwest Australian shelf, the South China Sea, and Indonesia, respectively). For this total the TPXO and GOT99 solutions again agree to within about 15% (see Table 2).

Summed over all shallow seas, all of the T/P dissipation estimates come up well short of the required total of 2.4 TW. With the exception of DW95 (which is a bit of an outlier, even for the global total), all of the additional T/P solutions considered here are consistent with the TPXO and GOT99 results presented by E-R, with total shallow sea dissipation around 1.6–1.8 TW. The remaining dissipation, required to match the well-determined global total must occur in the

Table 2. Area-Integrated Energy Dissipation

Area	TPXO				GOT99		Other T/P					TPXO4	Prev. Published	
	4a	4b	4c	SE	hf	nf	DW	CSR	FES	SR	TP3	prior	Miller	L-L
Shallow Sea Regions														
(1) Hudson Bay/Labrador	261	261	261	12	251	252	234	327	240	246	268	272	140	313
(2) European Shelf	208	203	204	31	191	199	166	178	184	172	259	297	167	271
(3) Yellow Sea	149	155	156	18	131	116	114	140	194	127	133	156	60	182
(4) NW Australian Shelf	158	172	179	29	143	152	92	76	108	94	154	170	192	131
(5) Patagonian Shelf	112	112	108	5	113	117	95	113	115	132	138	130	130	185
(6) NE Brazil	97	98	93	19	88	104	25	91	92	98	68	126	50	143
(7) Arctic/Norwegian Sea	70	67	70	20	87	90	73	84	84	93	52	157	35	21
(8) China Sea	46	54	17	18	56	72	41	56	19	46	43	41	6	–
(9) St. Law./Gulf Maine	60	59	59	6	58	62	50	42	37	36	66	69	31	–
(10) Andaman Sea	68	82	75	13	74	75	45	47	77	64	61	39	135	44
(11) E Africa/Arabia	23	40	43	20	36	57	36	105	56	23	30	7	18	–
(12) E Austr./N Guinea	49	61	48	14	68	74	19	58	95	62	33	75	27	34
(13) Antarctica	44	47	46	10	32	38	10	4	26	-7	25	36	–	60
(14) W North America	14	-17	5	16	43	71	10	55	44	41	53	44	110	68
(15) Bering Sea	29	35	35	6	47	47	32	30	37	33	71	29	246	75
(16) New Zealand	33	30	26	20	20	26	87	67	-1	81	45	75	–	32
(17) Okhotsk Sea	36	35	35	2	36	36	42	28	34	37	34	7	210	73
(18) India	33	23	28	13	34	37	9	29	22	16	36	38	100	29
(19) Indonesia	60	31	65	32	116	112	109	243	139	155	37	128	20	–
(20) Australia	15	19	15	8	49	54	8	15	49	0	7	16	0	–
(21) E North America	11	10	9	3	3	7	4	0	10	9	-6	6	0	–
(22) Carribean	12	15	16	8	13	14	24	18	26	24	18	3	3	–
(23) W Africa + Medn.	9	9	7	25	11	31	19	41	6	1	3	10	0	–
(24) Java-Sumatra	7	5	4	11	3	5	19	-4	7	7	9	3	0	–
(25) Kerguelen Plat	5	5	5	3	8	8	9	8	7	9	9	6	–	–
(26) E South America	12	18	19	5	0	6	7	23	-11	-3	0	5	0	–
(27) Japan	3	4	3	8	2	3	19	1	-11	8	9	4	43	–
(28) W South America	0	-2	2	8	2	7	-3	9	2	-1	36	7	4	–
4 + 8 + 19	(264)	(256)	(261)	(21)	(314)	(336)	(242)	(375)	(265)	(295)	(234)	(339)	(218)	–
Total Shallow	1625	1630	1633	56	1717	1876	1395	1885	1687	1602	1690	1956	1727	–
Deep Ocean Regions														
(A) Micronesia/Melanesia	100	79	112	22	102	95	136	93	59	135	113	19	–	–
(B) West Indian Ocean	108	97	91	23	110	90	134	89	80	129	92	5	–	–
(C) Mid-Atlantic Ridge	103	93	103	26	117	92	150	103	101	122	131	14	–	–
(D) W Pacific Trench	47	50	61	14	35	26	50	33	17	58	61	2	–	–
(E) Mid-Pacific Mt	45	43	39	16	27	28	14	39	27	25	51	2	–	–
(F) Polynesia	31	41	22	17	54	51	40	32	54	41	60	3	–	–
(G) East Pacific	41	75	54	17	39	24	57	33	40	54	5	2	–	–
(H) Hawaii	18	20	20	6	20	20	18	21	19	22	20	2	–	–
(I) Galapagos	15	18	16	8	11	6	13	9	13	13	-8	1	–	–
Remaining Ocean	305	284	285	72	214	139	346	106	322	279	244	8	–	–
Total Non-Shallow	813	802	802	54	729	570	958	558	733	879	769	58	–	–
Global Total	2438	2432	2435	17	2446	2446	2353	2443	2420	2481	2459	2014	1727	2010

deeper ocean. For the T/P based dissipation estimates this amounts to about 0.6–0.8 TW, or about 25–30% of the total.

The breakdown into some of the major areas of deep ocean dissipation is given in the second part of Table 2. The most significant areas (each accounting for approximately 100 GW in all estimates) are Micronesia and Melanesia in the western Pacific, the western Indian Ocean, and the Mid-Atlantic Ridge. The first of these areas contains a number of significant elongated topographic features including the Kermedec, Tonga, Lau, and Norfolk Ridges north of New Zealand. All of these are prominent in the dissipation maps of Plate 2. The second area includes the Mascerene and Southwest Indian Ridges and the Madagascar Plateau. These specific topographic features again generally show up as areas of enhanced dissipation in Plate 2. Other deep-ocean areas of note include the Hawaiian Ridge (consistently estimated to account for about 18–20 GW of dissipation), Polynesia (including the Tuamotu Ridge; about 40 GW), and the South Honshu Ridge (about 50 GW). There is also a significant amount of dissipation (generally around 200–300 GW) spread around the remaining open ocean. In fact, some of this remaining area (e.g., the North Atlantic between the northwest coast of Africa and the Mid-Atlantic Ridge) has moderately rough bottom topography and exhibits consistently elevated dissipation levels. Areas A-I of Figure 2 clearly do not contain all of the rough topography in the deep ocean. Note that the open ocean dissipation for the prior model is indeed very near zero, demonstrating that the noise associated with topographic features has little net effect on dissipation integrated over larger patches of ocean. We conclude from the comparisons of Table 2 and Plate 3 that the large-scale pattern of tidal dissipation does not depend strongly on details in the estimated tidal elevations, provided the fit to the T/P data is sufficiently good.

5.3. Sensitivity to Assumed Dynamics

To demonstrate the insensitivity of dissipation to prior dynamical assumptions, E-R compared results from five of the estimates summarized in Table 2 and Plate 3, TPXO.4a,b,c and GOT99hf,nf. These comparisons showed that the results are only weakly dependent on the assumed form for the friction $\mathcal{F}$ and the prior dynamical error covariance. We expand on these issues here, providing further details and discussion. We also address more explicitly the importance of proper weighting of the continuity equations for estimation of volume transports and consider possible effects of errors in the assumed bathymetry.

5.3.1. Sensitivity to assumed $\mathcal{F}$. The most obvious area of concern is that both the assimilation and weighted least squares methods require some sort of prior assumption about the dissipative term $\mathcal{F}$ in (5). To keep the problem linear for the weighted least squares approach, we restricted $\mathcal{F}$ to the simple linear drag law (22). By varying r one can easily test sensitivity of results to the assumed drag coefficient. Plate 4a shows dissipation estimates for the GOT99nf solution, computed by applying the least squares approach with $r = 0.0$ (i.e., no friction). The dissipation map is very similar to that obtained with the large friction parameter $r = 0.03$ (Plate 2c), although there is a slight tendency toward smaller open ocean dissipation in some areas (such as the North Atlantic) for the no-friction case. The similar appearance is confirmed more quantitatively by the area-integrated dissipation estimates of Table 2. Based on this comparison, and further experiments with intermediate values of r, we conclude that estimates of dissipation are relatively insensitive to the assumed linear friction coefficient over a wide range. In fact, the two values explicitly considered here are extreme and certainly bracket any plausible value of r.

The similarity of the GOT99 dissipation maps to those obtained with the assimilation approach provides further evidence for the insensitivity of our conclusions to prior assumptions about $\mathcal{F}$. For TPXO.4a we have assumed the quadratic drag law of (24). With this quadratic parameterization, energy dissipation by bottom drag can be large in shallow seas where current speeds are large, but is small in the open ocean (Plate 2a). Although the spatial distribution of dissipation resulting from this parameterization is quite different from that implied by a linear drag law with any value of r, essentially the same pattern of tidal energy dissipation is obtained when the T/P data are fit adequately.

5.3.2. Work done by errors in $\mathcal{F}$. For the TPXO.3 assimilation solution used by *Egbert* [1997], purely linear dynamics were used with the bottom drag again parameterized as (22) with $r = 0.03$. This relatively crude treatment of bottom drag was found to be the dominant source of error in the dynamics assumed by EBF, especially in open ocean areas where the linear drag law resulted in excessive dissipation [*Egbert*, 1997]. To correct for this deficiency in the prior model, and bring the elevations into agreement with the T/P data, significant misfit to the momentum balance equation (5) was required. The residuals ϵ_U to this equation can be viewed formally as an extra forcing term, which depends on the explicit assumed form for $\mathcal{F}$. If we evaluate dissipation directly using the estimated currents and the assumed dissipation parameterization

$$D_0 = \rho \mathbf{u} \cdot \mathcal{F}, \tag{26}$$

then the work done by these residuals

$$W_\epsilon = \rho \mathbf{u} \cdot \epsilon_U \tag{27}$$

must be included in the energy balance equation (12). If misspecification of $\mathcal{F}$ is the dominant error in the energy balance equation, then the true dissipation is approximately

$$D = D_0 - W_\epsilon. \tag{28}$$

Equation (28) clarifies how the dissipation estimates can be so insensitive to prior assumptions about the frictional stress: the dynamical residuals do work to effectively correct the assumed parameterized dissipation and bring the modeled elevations into agreement with the T/P data.

For TPXO.3. where the dissipation computed with the assumed parameterization (D_0) was too large in the open ocean, the work done by the dynamical residuals (W_ϵ) was

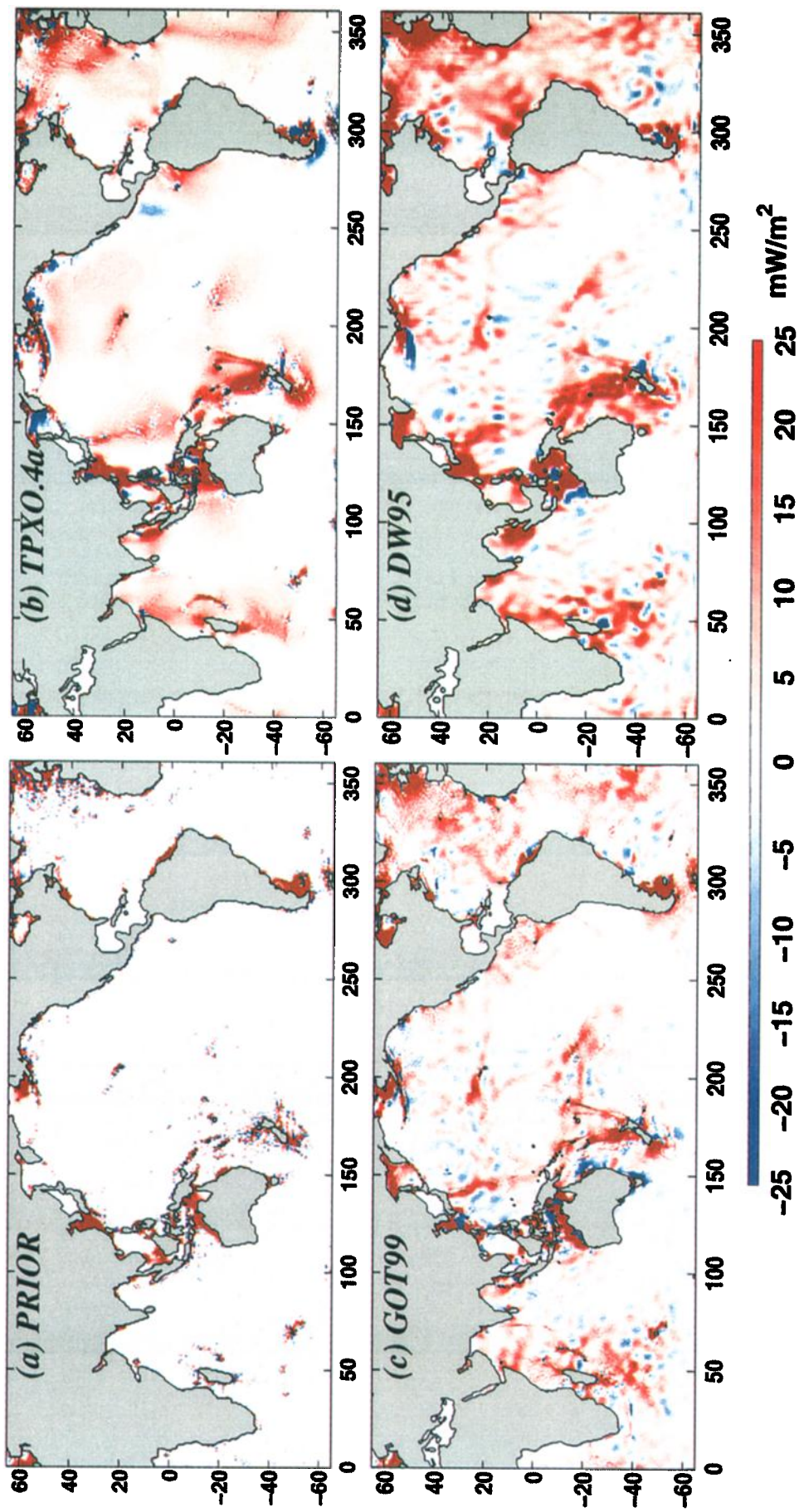

Plate 2. Tidal energy dissipation D estimated by applying (11)–(15), to four tidal elevation and current solutions. (a) For the hydrodynamic prior solution used for TPXO.4, dissipation is only significant in shallow water, consistent with the assumed quadratic bottom drag. Note the slightly noisy appearance (with small adjacent blue and red spots) near islands and other areas of poorly resolved bathymetry. Plates 2b-2d give estimates of D from three T/P M_2 tidal solutions. (b) Elevations and currents from the assimilation solution TPX0.4a, (c) GOT99 elevations with currents estimated using the least squares procedure of *Ray* [2001] with an assumed linear friction parameter $r = 0.03$, and (d) DW95 elevations with currents determined as for Plate 2c. All three of the T/P dissipation estimates show enhanced dissipation in the same general open ocean areas. Note that the color scale has been chosen to emphasize dissipation in the open ocean; the scale saturates in many shallow seas where dissipation is greatest.

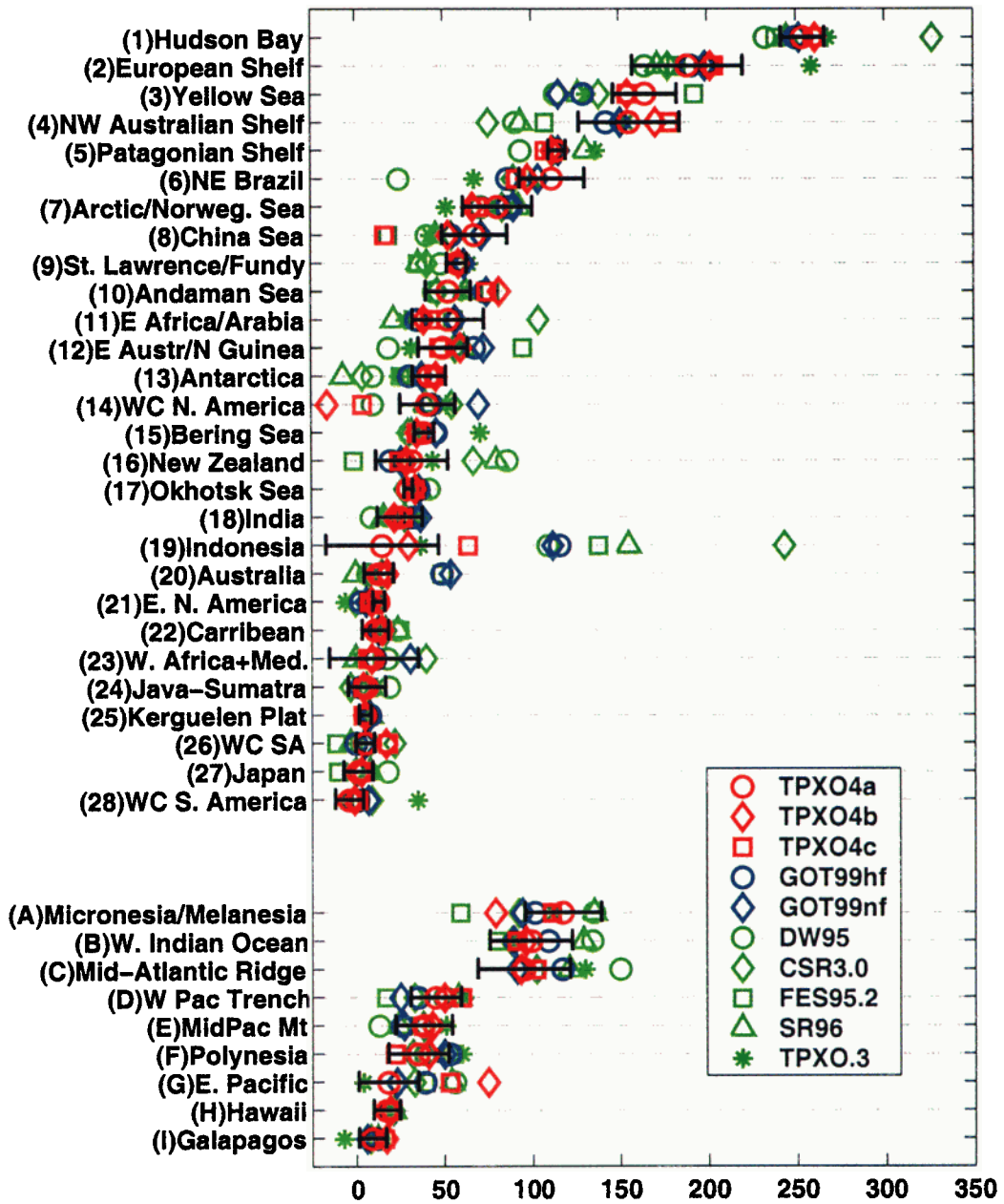

Plate 3. Plot of area-integrated dissipation estimates computed for the 10 tidal solutions of Table 2. Red symbols are used for the TPXO assimilation estimates, computed with three different dynamical error covariances. Blue symbols are used for the GOT99hf and GOT99nf estimates, computed with linear friction coefficients of $r = 0.03$ and $r = 0$, respectively. Green symbols are used for the other tidal solutions. The weighted least squares procedure with $r = 0.03$ was used to estimate volume transports for these other solutions (except for TPXO.3). Error bars were computed for the assimilation solution TPXO.4a using the Monte Carlo procedure described in the text.

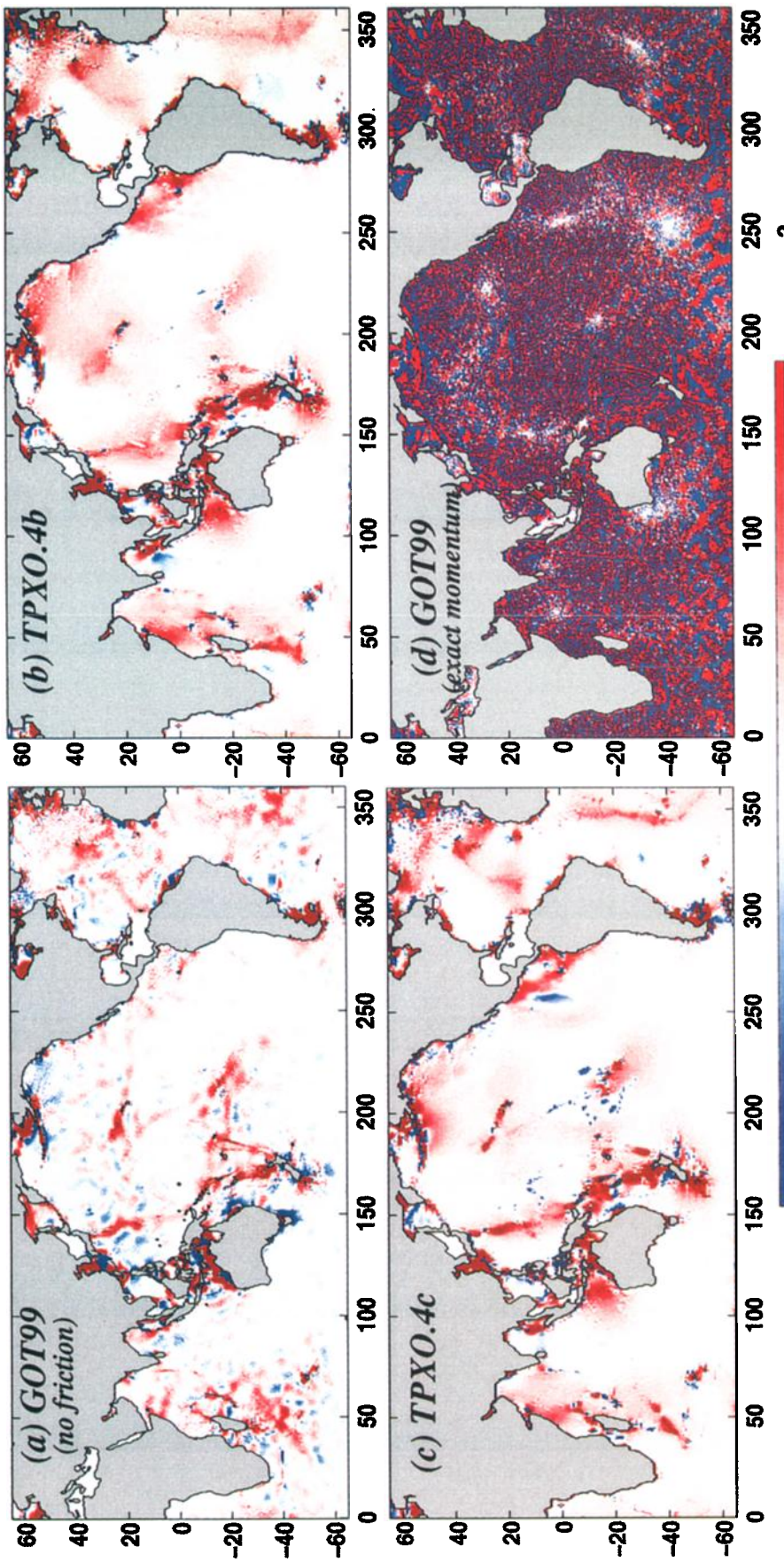

Plate 4. M_2 tidal energy dissipation maps for several variants on the solutions given in Plate 2. (a) GOT99nf with currents estimated as for GOT99hf of Plate 2c, but with linear friction coefficient $r = 0$. (b) TPXO.4b, a variant on the assimilation solution computed using a spatially uniform dynamical error variance, with a decorrelation length scale of 5 degrees. (c) TPXO.4c, computed with a dynamical error covariance tuned to emphasize areas of rough bottom topography. (d) Dissipation computed from GOT99 with currents estimated by exactly fitting the momentum equations and ignoring continuity. This last case yields results which are too noisy to be useful.

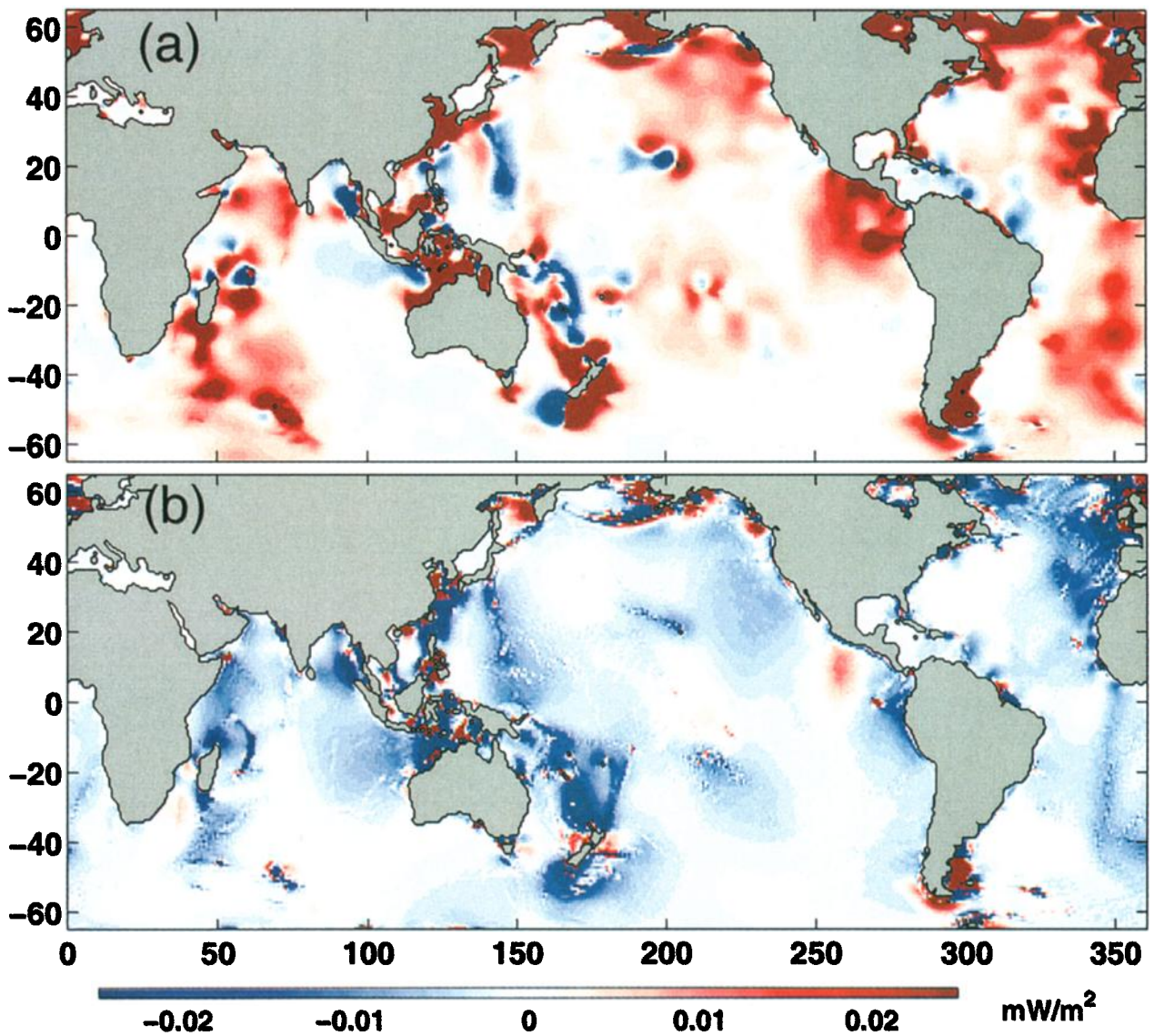

Plate 5. Work done by the dynamical residuals in the assimilation solutions. (a) For TPXO.3 a linear parameterization of bottom drag $\mathcal{F} = r\mathbf{U}/H$ was used with $r = 0.03$, making the assumed energy dissipation in the dynamical model too large in the deep ocean. To fit the altimeter data, residuals are required in the momentum equations. In this case these do work in the deep ocean to overcome the excessive drag. (b) For TPXO.4a a quadratic parameterization of $\mathcal{F}$ was used, so a priori there is little dissipation in the deep ocean. Now the residuals to the momentum equation do work in the opposite sense to increase dissipation almost everywhere in the open ocean.

generally positive, as illustrated in Plate 5a. In contrast, with the quadratic drag law used for the new TPXO.4a solution, D_0 in the open ocean is now very small and W_ϵ is almost always negative in deep water, especially over rough topography (Plate 5b). Starting from two extremes for D_0 (minimal and excessive open ocean dissipation), very different dynamical residuals, which do work in opposite senses, are required to fit the altimeter data. However, very similar estimates of dissipation D are obtained for both cases, providing very strong evidence that significant open ocean dissipation is required by the T/P altimeter data. Note that a similar analysis could be applied to the two weighted least squares dissipation estimates discussed in section 5.3.1. For the case $r = 0$, $D_0 \equiv 0$ and all dissipation in the final estimate arises from work done by the dynamical residuals. For the $r = 0.03$ case, the dynamical residuals in the open ocean generally do work in the opposite sense.

Between the assimilation and least squares approaches we have considered a very broad range of prior assumptions about the frictional dissipation $\mathcal{F}$, including both quadratic and linear drag laws with a wide range of drag coefficients. The generally good agreement between all of the dissipation maps demonstrates convincingly that our results are not unduly biased by prior assumptions about the nature of dissipation.

5.3.3. Sensitivity to assumed covariance. A second area of possible concern is the effect of the assumed prior error covariance on the estimated dissipation. This is most easily explored with the assimilation approach where the covariances are explicit.

For TPXO.4a a prior estimate of the magnitude of errors in the momentum equations (5) was obtained following the general analysis of EBF, but with allowance for the improvement we have made to the dynamics. For the solutions considered here the dynamical error variance is dominated by errors in the bathymetry and the effects of unresolved topography. As a result we have assumed a priori that errors in the dynamics are largest in places like the Hawaiian ridge or the western Pacific, where many islands and seamounts are not resolved by our coarse numerical grid. Although these prior assumptions about momentum equation errors may be reasonable, it is also possible that they bias our dissipation estimates. Away from topographic complications dynamical errors are assumed to be smaller, so that dynamical errors, and hence any required excess dissipation, will tend to be larger over rough topography. To assess this possibility we consider two variants on the preferred dynamical error covariance.

For the first case (TPXO.4b) we assume a spatially uniform dynamical error variance. As for TPXO.4a, decorrelation length scales are assumed to be 5 degrees. The resulting dissipation map is given in Plate 4b. Compared with TPXO.4a the dissipation estimates are slightly smoother, with features like the Hawaiian Ridge less distinct. However, the overall pattern is very similar, and all significant areas of enhanced dissipation remain. For the second case (TPXO.4c) we reduce the decorrelation length scale for the dynamical error covariance from 5 to 2.5 degrees. We also slightly modify the dynamical error variances from that used for TPXO.4a to increase error variances for individual grid cells containing significant fine scale variations in bottom topography. This modified error covariance $\Sigma_\mathbf{f}$ tends to put large errors (and thus potentially larger deviations of dissipation from the prior) in areas with topographic complications. The result (Plate 4c) is as expected, with topographic features such as ridges and island chains more sharply resolved (and also somewhat noisier). However, the general pattern remains essentially the same as for the other two cases. More quantitatively, Table 2 and Plate 3 show that details in the assumed dynamical error covariance $\Sigma_\mathbf{f}$ have very little effect on the large-scale pattern of dissipation.

5.3.4. Importance of mass conservation. We next consider the effect of relaxing the fit to the continuity equation. As noted in section 3, if the continuity equation is ignored and a linear drag parameterization is assumed, $\mathbf{U}$ can be estimated locally by solving two linear equations in two unknowns (i.e., (5)) at each point in the domain. In the least squares approach this entails setting the weight $w_\zeta = 0$ in (25). The resulting dissipation estimates are extremely noisy (Plate 4d). The reason is not hard to understand. The flux divergence may be written

$$\nabla \cdot \mathbf{P} = \rho g \nabla \cdot \langle \mathbf{U}(\zeta + \zeta_s) \rangle \tag{29}$$

$$= \rho g \langle (\zeta + \zeta_s) \nabla \cdot \mathbf{U} \rangle + \rho g \langle \mathbf{U} \cdot \nabla (\zeta + \zeta_s) \rangle . \tag{30}$$

Since computation of $\mathbf{U}$ already requires differentiation of the estimated elevation fields ζ, direct evaluation of $\nabla \cdot \mathbf{U}$ requires computing second derivatives of a measured field, which necessarily magnifies noise. However, if the continuity equation is enforced exactly, then

$$\nabla \cdot \mathbf{U} = -i\omega\zeta,$$

and the divergence of $\mathbf{U}$ need not be computed by actual differentiation. Second derivatives are thus completely avoided when (6) is fit exactly (as for the assimilation estimates) and significantly stabilized when only a small misfit is allowed (as for the least squares estimates).

As we have argued above, there are good a priori arguments for taking the continuity equation as a very strong constraint in deriving estimates of volume transports. The results of Plate 4d, and the argument of (29)–(30) shows that there are also good practical numerical reasons for enforcing mass conservation.

5.4. Inversion of Synthetic Data

As a definitive test of the ability of the T/P elevation data to constrain tidal dissipation, we applied the assimilation procedure to data generated from synthetic model runs. First, the nonlinear shallow water equations were solved by time-stepping on a $\frac{1}{4}^\circ$ grid, with several different input assumptions about friction and bathymetry. The tidal elevation fields were then sampled with a spatial and temporal

pattern equivalent to the altimeter, noise was added, and the inverse approach was used to compute transports and estimate dissipation. Since the synthetic tidal currents at the original $1/4°$ resolution are available, we can compare the actual dissipation in the numerical model with the inversion results. The procedure is essentially identical to that used for the Monte Carlo error bar calculation, except that instead of specifying random forcing and boundary conditions for the synthetic calculations, we ran the forward model with modified dynamics. In all cases for inversion of the synthetic data, we used the same $3/4°$ grid, with the bathymetry, dissipation, and dynamical error covariance used for TPXO.4a. By computing the synthetic "truth" with different bathymetry we can assess the importance of this additional source of uncertainty.

For the first set of synthetic runs the bathymetry was taken from the GTOPO30 database of *Smith and Sandwell* [1997] averaged onto a $1/4°$ grid. The bathymetry for these synthetic runs was thus of higher resolution but otherwise consistent with that used for the inversion. Dissipation was modified from the quadratic drag law used for the prior inverse solution in several ways. Starting from the prior solution, we computed a spatially varying linear drag coefficient that would produce the same dissipation as the quadratic law (for the prior solution currents). We then modified the drag coefficient in selected areas and reran the forward model with this modified linear friction. Plate 6 compares the actual synthetic and estimated dissipation maps for two variants on this procedure. For the first case (Plate 6a) all dissipation was confined to shallow seas, but the drag coefficient in some seas was modified (e.g., by setting it to 10% or 200% of the level calculated from the prior solution). For the second case (Plate 6b) dissipation was added to deeper ocean areas. To do this we followed the theory of *Sjöberg and Stigebrandt* [1992] to estimate an approximate linear drag coefficient that accounts for conversion of barotropic tidal energy to baroclinic modes. The required buoyancy frequency was computed from the climatology of *Levitus* [1999] and bathymetry (on a $5'$ resolution grid) was taken from *Smith and Sandwell* [1997]. Details of the calculation (which are somewhat involved but follow the development of *Sjöberg and Stigebrandt* [1992] closely) are not important for our discussion here. For this synthetic run there is significant dissipation over areas of rough topography in the open ocean where the theory predicts larger linear drag coefficients (Plate 6b).

Estimates of dissipation from inversion of the synthetic data are shown for the two cases in Plates 6c and 6d. The inversion results appear somewhat blurred, with some areas of negative dissipation, and a tendency to be noisiest in areas of rough topography. However, the overall agreement between actual (synthetic) and estimated dissipation is quite good for both cases. In particular, there is no significant dissipation in the deep ocean for the first case (Plates 6a and 6c). For the second case (Plates 6b and 6d) the areas of assumed deep ocean dissipation are reasonably captured in the estimates.

Figure 3 compares dissipation in the synthetic forward and inverse solutions for all of the shallow and deep sea areas of Figure 2. For reference we also show the dissipation computed for the prior solution (which was used as the "first guess" for inversion of the synthetic data). As can be seen, the modified linear drag coefficients result in significant changes in dissipation in some seas. After inversion of the synthetic data the estimates track the actual distribution of dissipation closely, with typical errors of the order of 5–10%. Fits are somewhat poorer for the North Australian Shelf, the China Sea, and Indonesia, which share boundaries in an area of complex bottom topography. However, the sum of dissipation in these areas for the synthetic run (490 GW) is quite close to the estimate from the inversion (497 GW). This behavior of the dissipation estimates is consistent with what we have seen with actual data for this complex area: although the total dissipation is well constrained, the partition between individual seas is not. Figure 3a confirms the impression of Plate 6, that there is little deep-ocean dissipation in the inverse estimate for the first case. The totals for all deep areas in Figure 3a are 38 GW for the actual synthetic solution, and -1 GW for the inverse estimate. For the second case of Figure 3b (where we have increased the drag coefficient in deep water) the deep-ocean totals are 484 GW for the synthetic, and 505 GW for the inverse estimate.

To test the effect of errors in bathymetry on dissipation estimates, we modified the bathymetry used for the synthetic calculations, while still using the standard bathymetry for the inversion. Results for two variants on this experiment are shown in Figure 3c and 3d. The spatially varying drag coefficient used for these runs is identical to that used for Figure 3a. For Figure 3c uncorrelated Gaussian errors with standard deviation 20% of the water depth were added to the standard $1/4°$ bathymetry. This makes the synthetic bathymetry quite rough, with a substantial number of extra seamounts everywhere in the ocean. For Figure 3d smooth random errors (with a decorrelation length scale of 5 degrees) were added to the standard bathymetry. For this experiment the relative perturbations to the bathymetry were a function of depth as follows: 25% for $H < 100$ m; 15% for $100 < H < 200$ m; 10% for $200 < H < 1000$ m; 6% for $1000 < H < 3000$ m; 3% for $H > 3000$. These relative error levels approximate the depth dependence of the statistics of differences between the older ETOPO5 [*National Geophysical Data Center*, 1992] database and GTOPO30 [*Smith and Sandwell*, 1997], and probably provide an upper bound on the magnitude of large-scale errors in the bathymetry we have used for the T/P dissipation estimates.

Uncorrelated errors in the bathymetry (i.e., with length scales below the grid resolution used for the inversion) have very little effect on the dissipation estimates (Figure 3c). In fact, results for this case are slightly better than when the inversion is done with the correct bathymetry (i.e., Figure 3a). The major improvement occurs for the three adjacent areas noted above (North Australian Shelf, China Sea, and Indonesia) and has most likely arisen by chance. The larger scale errors in the bathymetry used for Figure 3d lead to somewhat

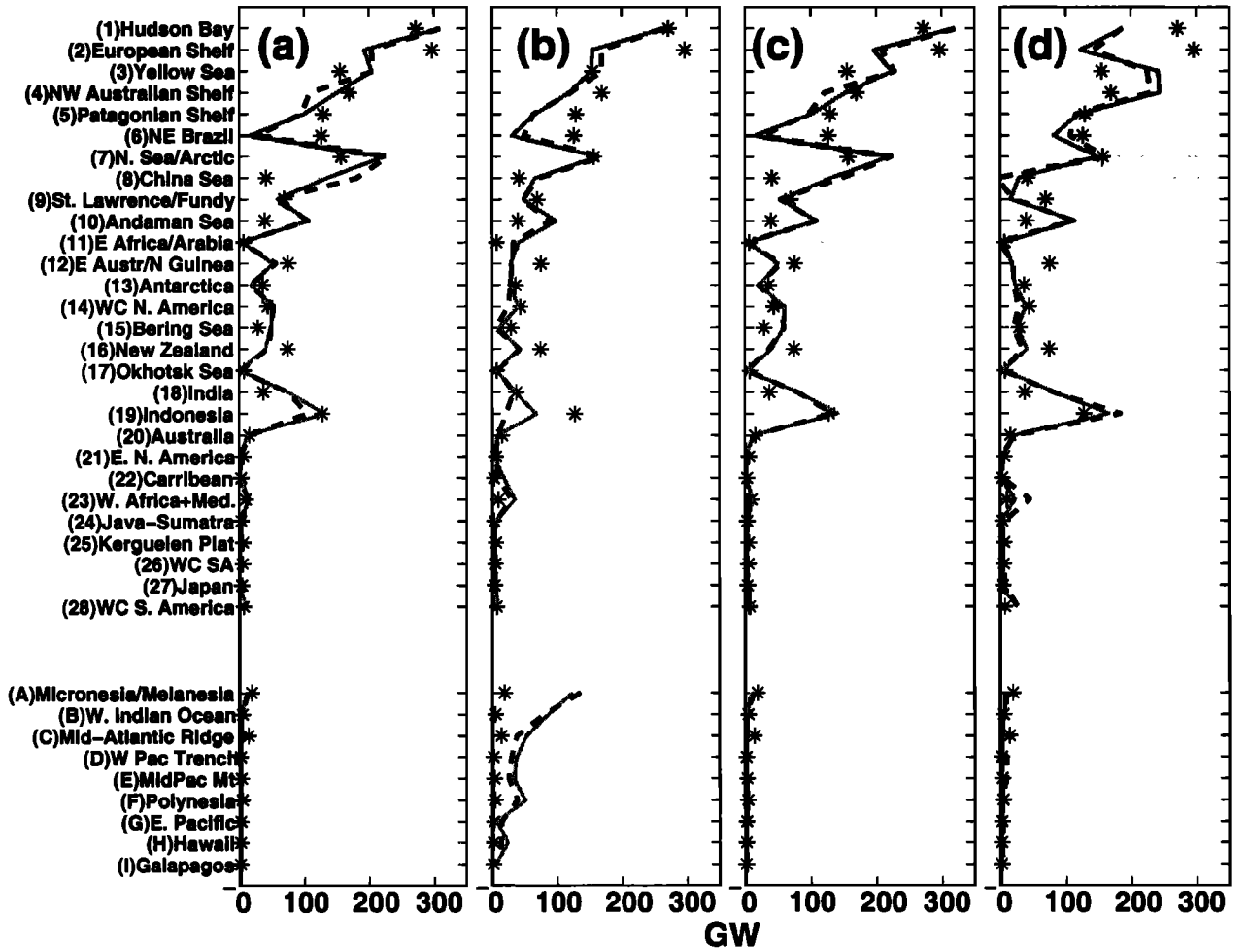

Figure 3. Comparison of actual (solid lines) and estimated (dashed lines) dissipation in shallow seas and deep ocean areas of Figure 2 for four synthetic runs. Symbols give dissipation for the prior hydrodynamic solution. (a) Modified linear drag, restricted to shallow seas (corresponding to the dissipation maps of Plates 6a and 6c). (b) Modified linear drag, with drag over rough topography in the deep ocean estimated following *Sjöberg and Stigebrandt* [1992] (Plates 6b and 6d). (c) As in Figure 3(a), but with 20% random errors in bathymetry (no spatial correlation). (d) As in Figure 3(a), but with spatially correlated (5 degree length scale) errors in bathymetry (amplitudes as given in text).

larger errors in the inverse estimates of dissipation. However, agreement between actual and estimated dissipation remains excellent.

We have run experiments with additional variations in drag laws and errors in bathymetry and boundary conditions in various combinations. The results presented here are typical. We conclude that the sampling pattern of the T/P data is sufficient to extract accurate estimates of the spatial localization of dissipation, with a resolution of 5° or so, even if the true bathymetry is only imperfectly known. The synthetic modeling results also suggest that small-scale unresolved topographic features do not substantially affect dissipation in either the synthetic runs or the inverse solutions.

6. Comparison to Other Dissipation Estimates

In Table 2 we include estimates of energy flux into shallow seas from *Miller* [1966] (regrouped where appropriate to correspond to the division of shallow seas of Figure 2), from our hydrodynamic prior solution, and from the finite element hydrodynamic solution FES94.1 [*Le Provost and Lyard*, 1997]. Note that for FES94.1 only the major sinks and the global integral were given in the original reference.

Dissipation in shallow seas computed from the purely hydrodynamic prior model tends to be larger than in the T/P estimates. The most significant differences are for the European Shelf and in the Arctic/Norwegian Sea, where dissipation in the prior solution is large, and about 50% above the empirical estimates. More generally, shallow sea dissipation in the prior and T/P solutions is similar, with a slight tendency to larger values in the prior. Agreement between the T/P estimates and the hydrodynamic calculations of *Le Provost and Lyard* [1997] is similar, also with a tendency toward larger shallow sea dissipation in the finite element model. The largest difference between the TPXO.4 prior solution and FES94.1 is in the Arctic/Norwegian Sea, which is 157 GW in the prior and only 21 GW for FES94.1. At least some of the difference between the hydrodynamic mod-

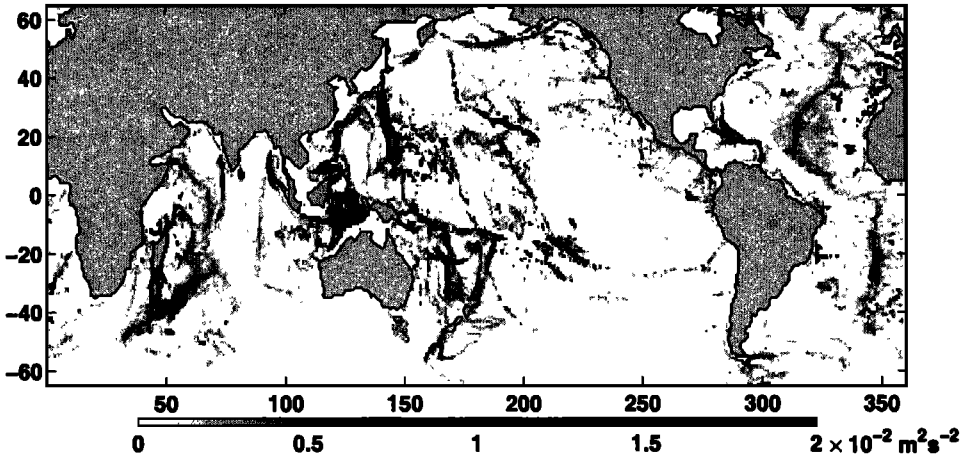

Figure 4. Magnitude of the vertically integrated body force resulting from flow of the barotropic tide over ocean bathymetry, estimated using the linear theory of *Baines* [1982]. This gives a qualitative indication of where forcing of internal tides is likely to be largest, which indeed is similar to areas of open–ocean energy dissipation in Plates 2 and 4.

els probably reflects differences in the shallow sea boundaries used for our calculations (Figure 2), and those used by *Le Provost and Lyard* [1997]. The total shallow sea dissipation for the two hydrodynamic models is in remarkably good agreement, at around 2.01 TW, well below the required global total of 2.4 TW.

Agreement between the T/P dissipation estimates and the energy flux estimates of *Miller* [1966] is poorer. Some areas that Miller estimated to be major sinks (the Bering Sea and Sea of Okhotsk, each estimated to be over 200 GW) are relatively insignificant (only 30-40 GW each) in all of our estimates. Some other significant sinks in Miller's compilation are also consistently reduced by a factor of 2 or more in the T/P estimates (the west coast of North America, shallow seas around India, Japan, the Andaman Sea). At the same time, Miller's estimates of flux into Hudson Bay and the Yellow Sea, two major sinks in all of the T/P estimates, are low by a factor of 2. Somewhat remarkably, given some of the large disagreements in specific areas, *Miller*'s [1966] estimate for the total shallow sea dissipation falls neatly within the range 1.6-1.8 TW which brackets most of the shallow sea dissipation estimates in Table 2.

Since *Miller*'s [1966] compilation, dissipation estimates have been published for a number of shallow seas. Most of these have been based on local hydrodynamic modeling, rather than actual in situ current and elevation data, as Miller used. For example, *Sündermann* [1977] used tide gauge data from the Aleutian arc to provide boundary conditions for a numerical model of the Bering Sea. His dissipation estimate for this area (29 GW) was significantly less than earlier estimates [*Jeffreys*, 1920; *Miller*, 1966]. The T/P estimates (for a slightly larger area) are in good agreement (29-47 GW for the TPXO and GOT99 solutions).

Unfortunately, there is rarely sufficient in situ data to adequately define open boundary conditions for the sort of large shallow sea or shelf areas considered here, so recourse must be made to a larger scale model. As a recent example of this sort of modeling study, *Glorioso and Flather* [1997] used open boundary conditions extracted from *Schwiderski* [1978] to model tides on the Patagonian shelf. For M_2 they estimated the dissipation to be 228 GW, in good agreement with the 245 GW estimate by *Cartwright and Ray* [1989] based on Geosat altimeter data, but more than twice the T/P estimates, all of which are near 115 GW. We suggest that the T/P estimates are preferable. *Cartwright and Ray* [1989] estimated dissipation using an approach similar to ours, but with currents computed without the extra constraint of mass conservation (6). As a result, these estimates should be expected to be very noisy, as indicated by Plate 4d. Similarly, there are also reasons to question the hydrodynamic results. *Glorioso and Flather* [1997] increased boundary amplitudes from the *Schwiderski* [1978] solution by 60% to obtain a better fit to coastal tide gauges, an amount that appears excessive given known errors in Schwiderski's solution [*Schrama and Ray,* 1994]. Based on experience with local finite element calculations for the Yellow Sea, *Lefevre et al.* [2000] concluded that regional dissipation estimates are very sensitive to the assumed open boundary conditions, which strongly influence energy flux into the model domain. In the Yellow Sea study open boundary conditions were taken from the FES94.2 solution. Tuning of the quadratic bottom drag coefficient used in the hydrodynamic model had very little effect on total dissipation, which remained close to the 182 GW found by *Le Provost and Lyard* [1997] for this area (Table 2; note that this is also close to the T/P estimates). Since boundary conditions for most published regional scale hydrodynamic models have been taken from older global solutions of relatively limited accuracy, conclusions from these numerical studies should be treated very cautiously. For the Patagonian Shelf the T/P dissipation estimates are probably more reliable, especially given the extremely good agreement between different tidal solutions and estimation approaches, and the small error bars.

By far the most careful empirical estimates of tidal ener-

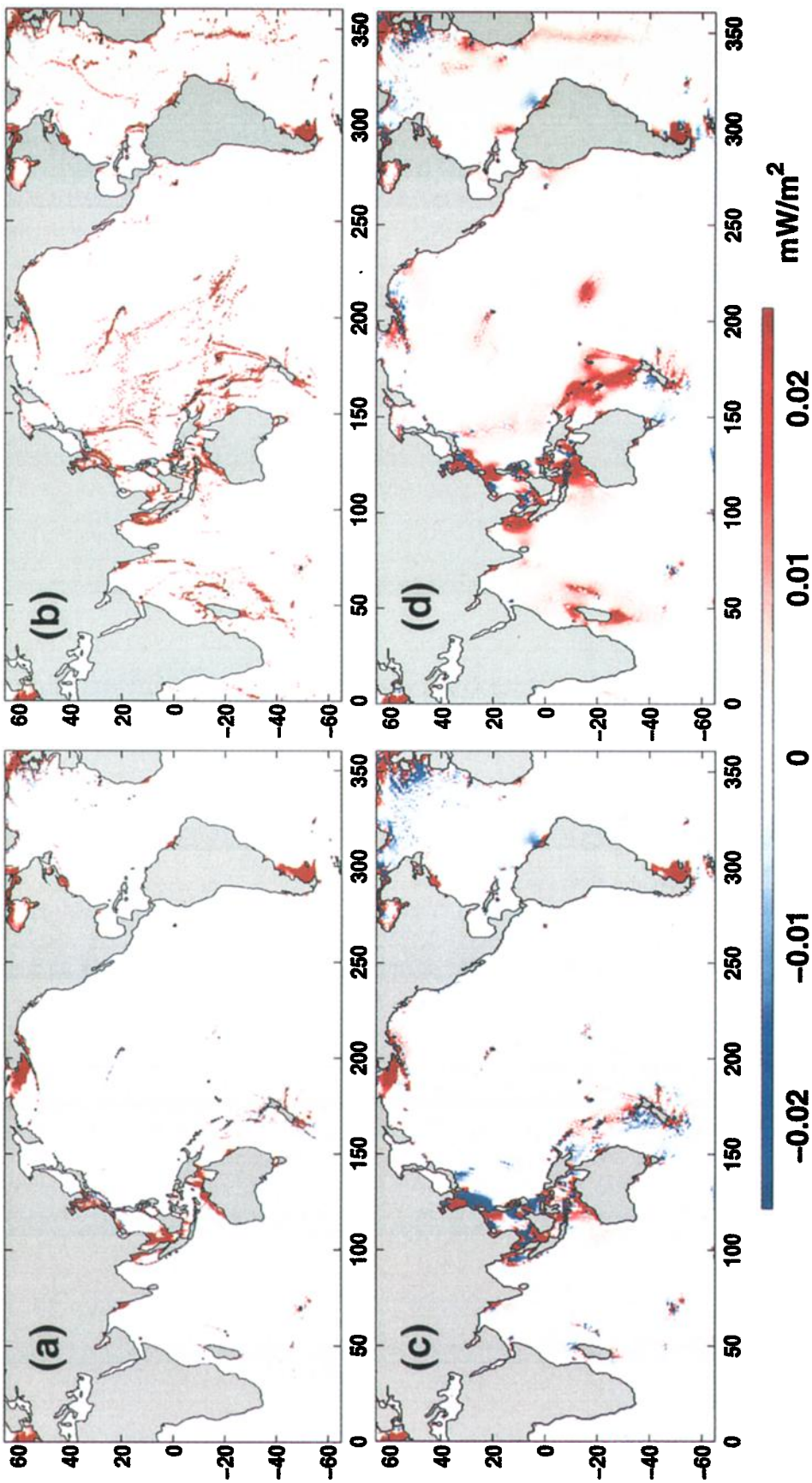

Plate 6. Dissipation computed from elevations and currents obtained by time stepping the shallow water equations using a linear friction parameterization with spatially varying drag coefficients. (a) The drag coefficient was estimated using the quadratic drag law (24) and currents from the prior solution and was then multiplied by randomly chosen factors in selected shallow seas. (b) An additional linear friction term was added in the open ocean to account for conversion to baroclinic modes by scattering over ocean bottom topography. Drag coefficients for this process were roughly estimated using the theory of *Sjöberg and Stigebrandt* [1992]. (c) and (d) Dissipation estimated by applying the generalized inverse approach to synthetic elevation data sampled (with the spatial and temporal pattern of the available T/P data) from the time–stepped solutions in Plates 6a and 6b respectively.

getics for a major sink are by *Cartwright et al.* [1980] for the European shelf area, including the North Sea and English Channel. Based on measurements from bottom pressure gauges and current moorings, this study estimated the flux onto the European shelf to be 250 GW. The part of the shelf considered roughly coincides with our shallow area 2. Our dissipation estimates are all somewhat lower, around 200 GW for the TPXO.4 and GOT99 solutions, but these allow for work done by the Moon and by the solid Earth. For TPXO.4a these work terms sum to −11 GW, and the actual flux into area 2 is 219 GW. More generally, about 10 GW should be added to the area 2 dissipation estimates of Table 2 for comparison to the energy flux estimates of *Cartwright et al.* [1980]. Allowing for the differences in the work terms, the altimetric estimates are thus consistently about 15% less than those obtained from the in situ data. The error bars for the TPXO.4a dissipation estimates are fairly large for this area (31 GW), and the uncertainty associated with the in situ estimates must be comparable, given the sparseness (especially in depth) of the current measurements. Allowing for these error bars, we conclude that the in situ and satellite estimates of energy flux are reasonably consistent.

Cartwright et al. [1980] also provided dissipation estimates of this area with finer geographic resolution. Flux into the southern part of the European Shelf, between Ireland and the Brittany coast, was estimated to be 190 GW. The flux through the English Channel into the North Sea was estimated to be 17 GW (with minimal flux north out of the Irish Sea), for a net flux into the English Channel and Irish Sea of 173 GW. The comparable net flux estimates obtained with TPXO solutions are in reasonably good agreement, ranging from 153–156 GW for the three covariances. However, agreement for the GOT99 solutions is poorer: 107 GW for GOT99hf and 138 for GOT99nf. The dissipation maps in this area are quite noisy (see Plate 2) and even coarse details in the bathymetry of this area are very poorly resolved in these global solutions. For example, England and Ireland are not even resolved as separate islands on these grids. The relatively poorer consistency of the T/P solutions among themselves, and with the in situ data, at this higher resolution is thus not surprising. The resolution of our global dissipation maps is really quite coarse, probably no better than 5° or so. This presents us with difficulties in comparing our dissipation estimates to local data-based studies of tidal energetics. With the exception of the *Cartwright et al.* [1980] study, these have been restricted to small geographic areas which are not reasonably resolved by our global scale study.

7. Discussion

Through experiments with real and synthetic data we have shown that T/P altimeter data provide sufficiently strong constraints on M_2 elevations to yield useful information about the global distribution of tidal energy dissipation. Provided the altimeter data and the continuity equation are fit sufficiently well when estimating volume transports, meaningful dissipation maps can be computed as the balance of barotropic energy flux divergence and local working by body and surface forces. Large-scale features in these maps depend only weakly on the specific T/P tidal elevation model used, prior assumptions about the nature of dissipation, details of prior covariances, and errors in the assumed bathymetry. All of the T/P dissipation estimates considered are in close agreement on the distribution of dissipation among shallow seas, and all exhibit similar large-scale patterns in the open ocean. Experiments with synthetic data reinforce the conclusion that the coverage and accuracy of the altimeter data are sufficient to allow accurate estimation of smoothed dissipation fields, even if the true bathymetry is not known or completely resolved. We stress again that mass conservation must be strongly enforced when estimating $\mathbf{U}$ to obtain these stable and reproducible results.

Results from all of our experiments strongly support the conclusion of E-R that approximately 25-30% of the M_2 energy dissipation (0.7 ± 0.15 TW) occurs in the deep ocean. In these areas, tidal velocities are too low for energy loss by bottom drag to be significant, at least with the traditional quadratic parameterization. *Zahel* [1980] has suggested that turbulent horizontal viscosity may also play an important role in tidal energetics. We have not explicitly included this term in our energy balance equation, but dissipation by this mechanism is implicitly accounted for in our generic stress $\mathcal{F}$. Synthetic calculations of the sort considered in section 5.4 show that even with the very large (and perhaps implausible) values for the coefficient of horizontal viscosity assumed by *Zahel* [1980] ($A_h = 2\times10^5$ m^2 s^{-1}), little dissipation would be expected in the deep ocean, so this mechanism also cannot account for the observed deep ocean dissipation.

While our estimates of barotropic energy balance cannot directly constrain dissipation mechanisms, the consistent spatial pattern in the deep ocean is highly suggestive. Much of the deep ocean dissipation is concentrated in areas of rough bottom topography, particularly over ridges and island arcs oriented perpendicular to barotropic tidal flows. This is exactly what would be expected if the energy loss from the barotropic tide is from generation of baroclinic modes as the stratified ocean is carried over steep topography.

It is instructive to compare our dissipation maps to a simple linear theory for generation of internal tides. *Baines* [1982] assumes linear equations for a rotating stratified inviscid fluid, and writes the tidal velocity as the sum of a barotropic component and a baroclinic perturbation $\mathbf{u} = \mathbf{u}_1 + \mathbf{u}_i$, and the perturbation of density from the local static profile ($\bar{\rho}$) as $\rho = \rho_1 + \rho_i$, where ρ_1 is the density perturbation caused by the barotropic motion. Linear equations for the internal wave motions $\mathbf{u}_i$, ρ_i are then readily derived:

$$\partial_t \mathbf{u}_i + \mathbf{f} \times \mathbf{u}_i + \rho_0^{-1}(\nabla p_i + \rho_i g\hat{\mathbf{z}}) = \mathbf{F}, \qquad (31)$$

where the depth-dependent body force $\mathbf{F}$ can be computed from the barotropic transport field ($\mathbf{U} = H\mathbf{u}_1$) and bathymetry H as

$$\mathbf{F} = \mathbf{U} \cdot [i\omega^{-1}N^2 z\nabla(1/H)]\hat{\mathbf{z}}, \qquad (32)$$

where $N = (-g\partial_z\bar{\rho}/\rho_0)^{1/2}$ is the buoyancy frequency. Equation (32) gives a simple expression for the barotropic

forcing of the baroclinic tide, which we have calculated using bathymetry from *Smith and Sandwell* [1997] averaged onto a 5′ grid, with N^2 estimated from the *Levitus* [1999] climatology, and volume transports from the TPXO.3 solution [*Egbert*, 1997].

The body force depends on the position in the water column z but has a constant phase at any location. To get some idea where the body force is large, we compute the integral over depth of $|\mathbf{F}|$. The resulting map of body force amplitude, plotted in Figure 4, is only a qualitative indicator of where conversion from barotropic to baroclinic modes should be energetically significant, since the actual conversion efficiency at any point will depend on the shape of the topography in a larger area. In particular, conversion should be most efficient where bottom slopes are tangent to the rays or characteristics of the internal waves [e.g., *Baines*, 1982]. Nonetheless, there is a good qualitative agreement between maps of dissipation and internal tide body force magnitude over most of the open ocean. Almost all of the areas where significant forcing of internal tides are predicted by the simple linear model indeed exhibit enhanced dissipation, and conversely.

The spatial pattern of dissipation mapped from the T/P data is also reasonably consistent with the calculations of conversion of barotropic tidal energy to baroclinic modes computed by *Sjöberg and Stigebrandt* [1992] using a simple theoretical model. We used formulae derived from this model to estimate linear drag coefficients due to topographic interactions in the open ocean for the synthetic model run of Plate 6b. The resulting pattern of dissipation is quite similar to the empirical T/P maps of Plates 2 and 4. The agreement of these maps with the synthetic inversion result of Plate 6d is even more striking. *Morozov* [1995] also estimated energy conversion to internal waves in the deep ocean, using a combination of the theory of *Baines* [1982] and direct measurements of internal tidal currents and vertical displacements. His maps are less detailed than those of *Sjöberg and Stigebrandt* [1992], but most of the areas where *Morozov* [1995] infers significant conversion also show up in the empirical dissipation maps.

The global total for the energetics of M_2 baroclinic conversion estimated by *Sjöberg and Stigebrandt* [1992] was 1.3 TW and by *Morozov* [1995] was 1.1 TW. This is rather higher than the roughly 0.7 TW estimate we obtain from the T/P data. We should note, however, that our estimates may be somewhat conservative. To avoid topographic complications, we have drawn boundaries for shallow seas well out in the deep ocean. At least some conversion to baroclinic modes may occur in the areas we have classified as shallow. This may particularly occur along continental shelves where submarine canyons and other along-shelf variations in bathymetry may significantly enhance local generation of internal tides [e.g., *Cummins and Oey,* 1997; *Petruncio et al.,* 1998], relative to the predictions of the two-dimensional model of *Baines* [1982]. The Andaman Sea (area 10 in Figure 2) provides an example of a shallow sea where there appears to be significant dissipation specifically near the outer edge (e.g., Plates 2b, 2c, 4a, and 4c), just where Figure 4 predicts large forcing of internal tides.

Many of the areas where we have mapped significant open ocean dissipation are also known generators of internal tides. Low-mode internal tides phase-locked to the barotropic tide can be seen as small modulations in amplitude and phase in along-track estimates of M_2 harmonic constants from T/P data [*Ray and Mitchum*, 1996, 1997]. Particularly clear examples are seen around the Hawaiian Ridge and the Tuamotu archipelago in the Pacific. Numerical modeling of the internal tide near Hawaii by *Merrifield and Holloway* [2000] is able to reproduce the surface pattern of low-mode internal tides quite well. Their estimated baroclinic energy flux is 9.7 GW. For the first baroclinic mode alone they obtain 6.0 TW, in reasonable agreement with 5.4 GW obtained by *Kang et al.* [2000] with a simple two-layer model. Our estimates of total barotropic dissipation in this area are exceptionally well constrained (presumably due to the isolation from other sinks and the lack of nearby topographic complications) to around 18-20 GW in all cases (Plate 3 and Table 2). Although larger than the estimated baroclinic radiation, the T/P estimates are not inconsistent, as the additional 10 GW of barotropic dissipation may generate local turbulence and mixing, rather than low-mode radiated internal waves.

Our results have obvious implications for how energy should be dissipated in numerical tidal models. More importantly, our finding that a significant fraction of tidal dissipation occurs over rough topography in the open ocean could have profound implications for vertical mixing in the abyssal ocean and possibly even for long-term variations in climate [*Munk and Wunsch*, 1998].

Munk [1966] and *Munk and Wunsch* [1998] estimate that a globally averaged diapycnal diffusivity of $10^{-4}\,\mathrm{m^2\,s^{-1}}$ is required to maintain the observed abyssal stratification. Without this degree of vertical mixing they argue that the meridional overturn circulation would shut down. Typical background diffusivities in the pelagic ocean estimated from ocean microstructure [*Gregg*, 1989] or tracer release data [*Ledwell et al.*, 1993] are of the order of only $10^{-5}\,\mathrm{m^2\,s^{-1}}$, but much of the required mixing across isopycnals may occur in localized hot spots which have been poorly sampled [*Munk*, 1966; *Armi*, 1978]. Recent in situ observations support this hypothesis [e.g., *Polzin et al.*, 1997; *Lueck and Mudge*, 1997; *Ledwell et al.*, 2000], with diffusivities as large as $10^{-3}\,\mathrm{m^2\,s^{-1}}$ observed in specific areas over rough topography. *Ledwell et al.* [2000] have further shown that measured turbulent energy dissipation rates are positively correlated with spring/neap variation in barotropic tidal velocities, suggesting that tides may provide at least some of the needed forcing.

Munk and Wunsch [1998] calculate that approximately 2 TW of mechanical energy must be provided to stir the ocean and maintain the observed stratification. As the working of the winds on the ocean surface is estimated to account for only about 1 TW [*Wunsch*, 1998], they further suggest that tides may provide about half the needed power. Extrapolating our results for M_2 to all other lunar and solar constituents

does yield about 1 TW, so the tides could indeed conceivably provide the additional power.

Calculations of *Samelson* [1998] and *Marotzke* [1998] suggest that the large-scale ocean circulation may be very sensitive to the spatial distribution of vertical mixing. An understanding of where and how this mixing occurs may thus be critical to realistic numerical modeling of long-term processes such as climate change. A more detailed understanding of the processes by which tidal energy is transfered to turbulent fluctuations in the deep ocean may thus turn out to be necessary for sensible modeling of climate. More speculatively, maintenance of stratification may depend on tidally forced mixing through a process that in turn depends on the stratification. Such an interaction between tides and stratification may be an important, but neglected, factor in long-term climate fluctuations. Further experimental and theoretical studies will be required to clarify the role of the tides, long seen as too periodic and regular to be interesting, in driving or modifying slower and more irregular ocean processes.

Appendix: Discrete Energy Balance Calculations

Harmonic constants of volume transport and elevation fields are defined on a discrete C grid, with ζ defined at the center of each cell, and U and V defined on the vertical and horizontal cell edges, respectively. Because the individual field components are defined at different grid nodes, and because we work in spherical coordinates, some care is required to estimate dissipation using (11)–(19).

The discrete gradient and divergence operators in spherical coordinates are defined in the usual way for the C grid. Thus the gradient operator maps naturally from the ζ nodes (cell centers) to the U/V nodes (cell edges). The energy flux vector $\mathbf{P} = g\rho\zeta H\mathbf{u}$ involves the product of fields defined at both edge and center nodes. To compute $\mathbf{P}$, we thus first average ζ laterally and vertically onto the cell edges and then compute products. The components of $\mathbf{P}$ are then defined on the U/V nodes, and the divergence of $\mathbf{P}$ can be calculated (on the ζ nodes) in the natural way. The calculation of the work done by the tide generating force (W) involves the dot product of $\mathbf{U}$ and $\nabla\Gamma$, two fields which are defined on the U/V nodes. We compute such dot products by summing the average of the U node products from each side of the cell and the V node products from the top and bottom, with weights determined by the metric terms appropriate for the sphere:

$$\begin{aligned}(\mathbf{U}^{(1)}\cdot\mathbf{U}^{(2)})_{i,j} &= [U^{(1)}_{i,j}U^{(2)}_{i,j} + U^{(1)}_{i+1,j}U^{(2)}_{i+1,j} \\ &+ \cos(\theta^{v}_{i,j})/\cos(\theta^{u}_{i,j})V^{(1)}_{i,j}V^{(2)}_{i,j} \\ &+ \cos(\theta^{v}_{i,j+1})/\cos(\theta^{u}_{i,j})V^{(1)}_{i,j+1}V^{(2)}_{i,j+1}]/2,\end{aligned}$$

where $\theta^{v}_{i,j}$ is the latitude of the bottom of the cell in column i and row j, and $\theta^{u}_{i,j}$ is the latitude of the cell center. Dot products computed in this way map from the U/V nodes to ζ nodes.

With these conventions for calculation of the discrete dot product, and of products between scalar (ϕ) and vector ($\mathbf{U}$) fields, scalars are always defined at the centers of the grid cells, and vector fields at the edges. It is readily verified that the usual vector identities such as $\nabla\cdot(\phi\mathbf{U}) = \phi\nabla\cdot\mathbf{U}+\mathbf{U}\cdot\nabla\phi$ hold exactly with these conventions. This guarantees exact equivalence between the surface and line integrals discussed in the text when these are evaluated numerically using the obvious metric terms.

Notation

Unless otherwise noted, the following values for various geophysical constants are employed throughout this paper (see main text for definitions).

GM 3.9860×10^{14} m^3 s^{-2}.
R 6.371×10^{6} m.
$\tilde{H}$ 0.63194 m (M_2).
ω 1.4052×10^{-4} s^{-1} (M_2).
Ω 7.2921×10^{-5} s^{-1}.
ρ 1035 kg m^{-3}.
ρ_e 5515 kg m^{-3}.
h_2 0.609.
k_2 0.302.
h'_n, k'_n are from *Farrell* [1972].

Acknowledgments. We thank Brian Beckley at NASA Goddard Space Flight Center for his help with the NASA Pathfinder altimeter data. GDE thanks Prof. Andrew Bennett for encouragement and many discussions that ultimately led to this work. This work was partially supported by the National Science Foundation (grants OCE-9633527 and OCE-9819518 to GDE), and by the National Aeronautics and Space Administration through the Topex/Poseidon and Jason-1 projects.

References

Armi, L., Some evidence for boundary mixing in the deep sea, *J. Geophys. Res., 83,* 1971–1979, 1978.

Baines, P. G., On internal tide generation models, *Deep Sea Res., 29,* 307–338, 1982.

Cartwright, D. E., Theory of ocean tides with application to altimetry, in *Satellite Altimetry in Geodesy and Oceanography,* edited by R. Rummel and F. Sansò, pp. 99–141, Springer-Verlag, New York, 1993.

Cartwright, D. E., and R. J. Tayler, New computations of the tide-generating potential, *Geophys. J. R. astron. Soc., 23,* 45–73, 1971.

Cartwright, D. E., A. C. Edden, R. Spencer, and J. M. Vassie, The tides of the northeast Atlantic Ocean, *Philos. Trans. R. Soc. London, 298,* 87–139, 1980.

Cartwright, D. E., and R. D. Ray, New estimates of oceanic tidal energy dissipation from satellite altimetry, *Geophys. Res. Lett., 16,* 73–76, 1989.

Cartwright, D. E., and R. D. Ray, Energetics of global ocean tides from Geosat altimetry, *J. Geophys. Res., 96,* 16,897–16,912, 1991.

Christodoulidis, D. C., D. E. Smith, R. G. Williamson, and S. M. Klosko, Observed tidal braking in the Earth/Moon/Sun system, *J. Geophys. Res., 93,* 6216–6236, 1988.

Cummins, P. F., and L. Y. Oey, Simulation of barotropic and baroclinic tides off Northern British Columbia, *J. Phys. Oceanogr., 27,* 762–781, 1997.

Desai, S. D., and J. M. Wahr, Empirical ocean tide models esti-

mated from TOPEX/Poseidon altimetry, *J. Geophys. Res., 100,* 25,205–25,228, 1995.

Dushaw, B. D., G. D. Egbert, P. F. Worcester, B. D. Cornuelle, B. M. Howe, and K. Metzger, A TOPEX/POSEIDON global tidal model (TPXO.2) and barotropic tidal currents determined from long range acoustic transmissions, *Prog. Oceanogr., 40,* 337–369, 1997.

Egbert, G. D., Tidal data inversion: Interpolation and inference, *Prog. Oceanogr., 40,* 81–108, 1997.

Egbert, G. D., and A. F. Bennett, Data assimilation methods for ocean tides, in *Modern Approaches to Data Assimilation in Ocean Modeling*, edited by P. Malonottte-Rizzoli, pp. 147–179, Elsevier Sci., New York, 1996.

Egbert, G. D., and R. D. Ray, Significant tidal dissipation in the deep ocean inferred from satelite altimeter data, *Nature, 405,* 775–778, 2000.

Egbert, G. D., and S. Y. Erofeeva, Efficient inverse modeling of barotropic ocean tides, *J. Atmos. Ocean. Tech.*, in press, 2001.

Egbert, G. D., A. F. Bennett, and M. G. G. Foreman, TOPEX/POSEIDON tides estimated using a global inverse model, *J. Geophys. Res., 99,* 24,821–24,852, 1994.

Farrell, W. E., Deformation of the Earth by surface loads, *Rev. Geophys., 10,* 761–797, 1972.

Garrett, C., Tides in gulfs, *Deep Sea Res., 22,* 23–35, 1975.

Gill, A. E., *Atmosphere-Ocean Dynamics*, Academic, San Diego, Calif., 1982.

Glorioso, P. D., and R. A. Flather, The Patagonian shelf tides, *Prog. Oceanogr., 40,* 263–283, 1997.

Gregg, M. C., Scaling turbulent dissipation in the thermocline, *J. Geophys. Res., 94,* 9686–9698, 1989.

Hansen, K. S., Secular effects of oceanic tidal dissipation on the Moon's orbit and the Earth's rotation, *Rev. Geophys., 20,* 457–480, 1982.

Haurwitz, B., and A. D. Cowley, The lunar barometric tide, its global distribution and annual variation, *Pure Appl. Geophys., 77,* 122–150, 1969.

Hendershott, M. C., The effects of solid earth deformation on global ocean tides, *Geophys. J. R. astron. Soc., 29,* 389–402, 1972.

Hendershott, M. C., Numerical models of ocean tides, in *The Sea*, vol. 6, *Marine Modelling,* edited by E. Goldberg et al., pp. 47–95, John Wiley, New York, 1977.

Huthnance, J. M., Internal tides and waves near the continental shelf edge, *Geophys. Astrophys. Fluid Dyn., 48,* 81–106, 1989.

Jeffreys, H., Tidal friction in shallow seas, *Philos. Trans. R. Soc. London, Ser. A, 221,* 239–264, 1920.

Kagan, B. A., and N. V. Shkutova, On the effect of ocean tides on gravitational tides in the atmosphere, *Okeanologiya, 25,* 193–200, 1985.

Kagan, B. A., and J. Sündermann, Dissipation of tidal energy, paleotides, and evolution of the Earth-Moon system, *Adv. Geophys., 38,* 179–266, 1996.

Kang, S. K., M. G. G. Foreman, W. R. Crawford, and J. Y. Cherniawsky, Numerical modeling of internal tide generation along the Hawaiian Ridge, *J. Phys. Oceanogr., 30,* 1083–1098, 2000.

Lambeck, K., Tidal dissipation in the oceans: Astronomical, geophysical, and oceanographic consequences, *Philos. Trans. R. Soc. London. Ser. A, 287,* 545–594, 1977.

Ledwell, J. R., A. J. Watson, and C. S. Law, Evidence for slow mixing across the pycnocline from an open ocean tracer release experiment, *Nature, 364,* 701–703, 1993.

Ledwell, J. R., E. T. Montgomery, K. T. Polzin, L. C. St. Laurent, R. W. Scmitt, and J. M. Toole, Evidence for enhanced mixing over rough topography in the abyssal ocean, *Nature, 403,* 179–182, 2000.

Lefevre, F., C. Le Provost, and F. H. Lyard, How can we improve a global ocean tide model at a regional scale? A test on the Yellow Sea and the East China Sea, *J. Geophys. Res., 105,* 8707–8725, 2000.

Le Provost, C., and F. Lyard, Energetics of the barotropic ocean tides: An estimate of bottom friction dissipation from a hydrodynamic model, *Prog. Oceanogr., 40,* 37–52, 1997.

Le Provost, C., M. L. Genco, F. Lyard, P. Vancent, and P. Canceil, Spectroscopy of the world ocean tides from a hydrodynamic finite element model, *J. Geophys. Res., 99,* 24,777–24,797, 1994.

Le Provost, C., F. Lyard, J.-M. Molines, M. L. Genco, and F. Rabilloud, A hydrodynamic model improved by assimilating a satellite altimeter derived data set, *J. Geophys. Res., 103,* 5513–5529, 1998.

Levitus, S., Levitus 1982 annual climatology from DODS datasets Goddard DAAC, NASA, Greenbelt, Md., 1999.

Lueck, R. G., and T. D. Mudge, Topographically induced mixing around a shallow seamount, *Science, 276,* 1831–1833, 1997.

Marotzke, J., Boundary mixing and the dynamics of three-dimensional thermohaline circulations, *J. Phys. Oceanogr.*, 28, 1713–1728, 1998.

McCarthy, D. D. (Ed.), *IERS Conventions (1996), Tech. Note 21,* 95 pp., Int. Earth Rotation Serv., Obs. de Paris, Paris, 1996.

Merrifield, M. A. and P. E. Holloway, Numerical simulations of M_2 internal tide generation at the Hawaiian Ridge (abstract), *Eos Trans. AGU, 81(48),* Fall Meet. Suppl., OS72B-20, 2000.

Miller, G. R., The flux of tidal energy out of the deep ocean, *J. Geophys. Res., 71,* 2485–2489, 1966.

Morozov, E. G., Semidiurnal internal wave global field, *Deep Sea Res., 42,* 135–148, 1995.

Munk, W. H., Abyssal recipes, *Deep Sea Res., 13,* 707–730, 1966.

Munk, W. H., Once again: Once again – tidal friction, *Prog. Oceanog., 40,* 7–36, 1997.

Munk, W. H., and G. J. F. MacDonald, *The Rotation of the Earth,* 323 pp., Cambridge Univ. Press, New York, 1960.

Munk, W. H., and C. Wunsch, Abyssal recipes II: Energetics of tidal and wind mixing, *Deep Sea Res., 45,* 1977–2010, 1998.

National Geophysical Data Center, GEODAS CD-ROM worldwide marine geophysical data, *Data Announce. 92-MGG-02,* Natl. Oceanic and Atmos. Admin., U.S. Dep. of Commer., Boulder, Colo., 1992.

Petruncio, E. T., L. K. Rosenfeld, and J. D. Paduan, Observations of internal tides in Monterey Canyon, *J. Phys. Oceanogr., 28,* 1873–1903, 1998.

Platzman, G. W., Planetary energy balance for tidal dissipation, *Rev. Geophys., 22,* 73–84, 1984.

Platzman, G. W., The role of Earth tides in the balance of tidal energy, *J. Geophys. Res., 90,* 1789–1793, 1985.

Platzman, G. W., An observational study of energy balance in the atmospheric lunar tide, *Pure Appl. Geophys., 137,* 1–33, 1991.

Polzin, K. L., J. M. Toole, J. R. Ledwell, and R. W. Schmitt, Spatial variability of turbulent mixing in the abyssal ocean, *Science, 276,* 93–96, 1997.

Ray, R. D., Tidal energy dissipation: Observations from astronomy, geodesy, and oceanography, in *The Oceans*, edited by S. Majumdar et al., pp. 171–185, Pa. Acad. of Sci., Easton, Pa., 1994.

Ray, R. D., Ocean self-attraction and loading in numerical tidal models, *Mar. Geod., 21,* 181–192, 1998.

Ray, R. D., A global ocean tide model from Topex/Poseidon altimetry: GOT99.2, NASA Tech. Memo. 1999-209478, 1999.

Ray, R. D., Inversion of oceanic tidal currents from measured elevations, *J. Mar. Syst., 28,* 1–18, 2001.

Ray, R. D., and G. T. Mitchum, Surface manifestation of internal tides generated near Hawaii, *Geophys. Res. Lett., 23,* 2101–2104, 1996.

Ray, R. D., and G. T. Mitchum, Surface manifestation of internal tides in the deep ocean: Observations from altimetry and island gauges, *Prog. Oceanogr., 40,* 135–162, 1997.

Ray, R. D., R. J. Eanes, and B. F. Chao, Detection of tidal dissipation in the solid Earth by satellite tracking and altimetry, *Nature, 381,* 595–597, 1996.

Ray, R. D., R. J. Eanes, and F. G. Lemoine, Constraints on energy

dissipation in the earth's body tide from satellite tracking and altimetry, *Geophys. J. Int., 144*, 471–480, 2001.

Samelson, R. M., Large scale circulation with locally enhanced vertical mixing, *J. Phys. Oceanogr., 28*, 712–726, 1998.

Schrama, E. J. O., and R. D. Ray, A preliminary tidal analysis of TOPEX/POSEIDON altimetry, *J. Geophys. Res., 99*, 24,799–24,808, 1994.

Schwiderski, E. W., Global ocean tides, I, a detailed hydrodynamical interpolation model, *Rep NSWC/DL TR-3866*, Nav. Surface Weapons Cent., Silver Spring, Md., 1978.

Shum, C. K., et al., Accuracy assessment of recent ocean tide models, *J. Geophys. Res., 102*, 25,173–25,194, 1997.

Sjöberg, B., and A. Stigebrandt, Computations of the geographical distribution of the energy flux to mixing processes via internal tides and the associated vertical circulation in the ocean, *Deep Sea Res., 39*, 269–291, 1992.

Smith, W. H. F., and D. T. Sandwell, Global sea floor topography from satellite altimetry and ship depth soundings, *Science, 277*, 1956–1962, 1997.

Sündermann, J., The semi-diurnal principal lunar tide M_2 in the Bering Sea, *Dtsch. Hydrogr. Z., 30*, 91–101, 1977.

Taylor, G. I., Tidal friction in the Irish Sea, *Philos. Trans. R. Soc. London, Ser. A, 220*, 1–33, 1919.

Williams, J. G., X X Newhall, and J. O. Dickey, Diurnal and semidiurnal tidal contributions to lunar secular acceleration (abstract), *Eos, Trans. AGU, 73(43)*, Fall Meeting Suppl., 126, 1992.

Williams, J. G., D. H. Boggs, C. F. Yoder, J. T. Ratcliff, and J. O. Dickey, Lunar rotational dissipation in solid body and molten core, *J. Geophys. Res.*, in press, 2001.

Wunsch, C., Internal tides in the ocean, *Rev. Geophys., 13*, 167–182, 1975.

Wunsch, C., Comment on R. N. Stewart's "Physical Oceanography to the end of the twentieth century," in *Quo Vadimus: Geophysics for the Next Generation, Geophys. Monogr. Ser.*, vol. 60, edited by G. D. Garland and J. Apel, p. 69, AGU, Washington, D.C., 1990.

Wunsch, C. The work done by the wind on the ocean circulation, *J. Phys. Oceanogr., 28*, 2331–2339, 1998.

Zahel, W., Mathematical modelling of global interaction between ocean tides and Earth tides, *Phys. Earth Planet. Inter., 21*, 202–217, 1980.

Zahel, W., Assimilating ocean tide determined data into global tidal models *J. Mar. Syst. 6*, 3-13, 1995.

Zschau, J., Tidal friction in the solid Earth: Loading tides versus body tides, in *Tidal Friction and the Earth's Rotation*, edited by P. Brosche and J. Sündermann, pp. 62–94, Springer-Verlag, New York, 1978.

Zschau, J., Tidal friction in the solid Earth: Constraints from the Chandler Wobble period, in *Space Geodesy and Geodynamics*, edited by A. Anderson and A. Cazenave, pp. 315–344, Academic, San Diego, Calif., 1986.

G. D. Egbert, College of Oceanic and Atmospheric Sciences, Ocean. Admin. Bldg. 104, Oregon State University, Corvallis OR 97331-5503, USA. (egbert@oce.orst.edu)

R. D. Ray, NASA Goddard Space Flight Center, Code 926, Greenbelt, MD 20771, USA. (richard.ray@gsfc.nasa.gov)

(Received November 1, 2000; revised May 10, 2001;
accepted May 24, 2001.)